



## The H1 Liquid Argon Calorimeter System

The H1 Calorimeter Group

ISSN 0418-9833

NOTKESTRASSE 85 - 22603 HAMBURG

DESY behält sich alle Rechte für den Fall der Schutzrechtserteilung und für die wirtschaftliche Verwertung der in diesem Bericht enthaltenen Informationen vor.

DESY reserves all rights for commercial use of information included in this report, especially in case of filing application for or grant of patents.

To be sure that your preprints are promptly included in the  
HIGH ENERGY PHYSICS INDEX,  
send them to (if possible by air mail):

**DESY  
Bibliothek  
Notkestraße 85  
22603 Hamburg  
Germany**

**DESY-IfH  
Bibliothek  
Platanenallee 6  
15738 Zeuthen  
Germany**

## The H1 Liquid Argon Calorimeter System

### H1 Calorimeter Group

#### Abstract

The liquid argon calorimeter of the H1 detector presently taking data at the HERA *ep*-collider at DESY, Hamburg, is described here. The main physics requirements and the most salient design features relevant to this calorimeter are given.

The aim to have smooth and hermetic calorimetric coverage over the polar angular range  $4^\circ \leq \theta \leq 154^\circ$  is achieved by a single liquid argon cryostat containing calorimeter stacks structured in wheels and octants for easy handling. The absorber materials used are lead in the electromagnetic part and stainless steel in the hadronic part. The read-out system is pipelined to reduce the dead time induced by the high trigger rate expected at the HERA collider where consecutive bunches are separated in time by 96 ns.

The main elements of the calorimeter, such as the cryostat, with its associated cryogenics, the stack modules, the read-out, calibration and trigger electronics as well as the data acquisition system are described.

Performance results from data taken in calibration runs with full size H1 calorimeter stacks at a CERN test beam, as well as results from data collected with the complete H1 detector using cosmic rays during the initial phase of *ep* operations are presented.

The observed energy resolutions and linearities are well in agreement with the requirements.

Submitted to NIM

- B. Andrieu<sup>11</sup>, A. Babayev<sup>7</sup>, J. Bán<sup>6</sup>, E. Banas<sup>2,9</sup>, E. Barrelet<sup>12</sup>, U. Bassler<sup>12</sup>, D. Bedere<sup>12</sup>, R. Bernard<sup>4</sup>, G. Bernardi<sup>12</sup>, R. Bernier<sup>10</sup>, M. Besançon<sup>4</sup>, J.-C. Biasci<sup>10</sup>, E. Binder<sup>5</sup>, F. Blouzo<sup>12</sup>, H. Blume<sup>9</sup>, K. Borras<sup>3</sup>, V. Boudry<sup>11</sup>, F. Brasse<sup>5</sup>, D. Breton<sup>10</sup>, H. Brettel<sup>9</sup>, V. Brisso<sup>12</sup>, D. Bruncko<sup>9</sup>, U. Buchner<sup>3</sup>, A. Busata<sup>11</sup>, G. Buschhorn<sup>9</sup>, A. J. Campbell<sup>12</sup>, T. Carli<sup>11</sup>, F. Charal<sup>12</sup>, R. Chase<sup>10</sup>, M. Colombo<sup>3</sup>, Ch. Coutures<sup>4</sup>, A. Coville<sup>12</sup>, G. Cozzika<sup>4</sup>, J. Cvach<sup>11</sup>, M. Danil<sup>12</sup>, M. David<sup>4</sup>, J. David<sup>12</sup>, B. Delcourt<sup>10</sup>, L. Del Buono<sup>12</sup>, F. Descamps<sup>12</sup>, M. Devel<sup>10</sup>, A. DeRoee<sup>12</sup>, P. Dingus<sup>11</sup>, K. Djidi<sup>4</sup>, A. Drescher<sup>3</sup>, U. Dretzler<sup>3</sup>, M. Drewe<sup>3</sup>, J. Duboc<sup>12</sup>, F. Dupon<sup>12</sup>, V. Efremenko<sup>7</sup>, F. Eisele<sup>5</sup>, G. Ernst<sup>3</sup>, G. Falley<sup>5</sup>, R. Fang<sup>12</sup>, J. Feltesse<sup>4</sup>, Z. Y. Feng<sup>12</sup>, J. Fe<sup>12</sup>, J. Ferenc<sup>5</sup>, W. Flauger<sup>5,1</sup>, G. Flügge<sup>1</sup>, J. Formánek<sup>14</sup>, W. Fröchtenicht<sup>9</sup>, K. Gamberding<sup>12</sup>, J. Gayler<sup>5</sup>, I. Giesgen<sup>1</sup>, J. Godlewski<sup>2</sup>, L. Goerlich<sup>2</sup>, M. Goldberg<sup>12</sup>, P. Gorichev<sup>7</sup>, L. Goss<sup>12</sup>, R. Grässer<sup>1</sup>, C. Gregory<sup>11</sup>, H. Greif<sup>9</sup>, G. Grindhammer<sup>9</sup>, M. Haguenauer<sup>11</sup>, L. Hajduk<sup>2</sup>, O. H. He<sup>12</sup>, P. Hartz<sup>3</sup>, R. Haydar<sup>10</sup>, I. Herynek<sup>13</sup>, W. Hildesheim<sup>12</sup>, J. Hladky<sup>13</sup>, J. Huber<sup>9</sup>, N. Huo<sup>12</sup>, J.-F. Huppert<sup>12</sup>, D. Imbault<sup>12</sup>, M.-A. Jabiol<sup>4</sup>, A. Jacholkowska<sup>10</sup>, M. Jaffe<sup>10</sup>, J. Jeanjean<sup>12</sup>, H. Jung<sup>1</sup>, C. Kiesling<sup>9</sup>, M. Kolarer<sup>3</sup>, H. Kolanoski<sup>3</sup>, J. Koll<sup>5</sup>, V. Korbel<sup>5</sup>, M. Korn<sup>3</sup>, W. Kraja<sup>12</sup>, M. Kubantsev<sup>7</sup>, J.-P. Kubenka<sup>9</sup>, H. Küster<sup>5</sup>, M. Kuhn<sup>9</sup>, T. Kurča<sup>6</sup>, J. Kurzhöfer<sup>3</sup>, J.-F. Lapp<sup>12</sup>, H. Laskus<sup>9</sup>, M. Lemler<sup>2</sup>, U. Lenhardt<sup>3</sup>, P. Loch<sup>5</sup>, D. Liers<sup>9,1</sup>, E. Malinowski<sup>8</sup>, J. Mar<sup>12</sup>, F. Martin<sup>12</sup>, J. Martyniak<sup>2</sup>, T. Merz<sup>5</sup>, S. Mikocki<sup>2</sup>, E. Monnier<sup>12</sup>, B. Montés<sup>11</sup>, P. Mur<sup>12</sup>, V. Nagovizin<sup>7</sup>, P. Nayman<sup>12</sup>, A. Nepepivo<sup>7</sup>, H.K. Nguyen<sup>12</sup>, H. Novakova<sup>13</sup>, G. Nowo<sup>12</sup>, H. Oberlack<sup>3</sup>, U. Obrock<sup>3</sup>, P. Pailler<sup>4</sup>, J.-Y. Pary<sup>11</sup>, C. Pascaud<sup>10</sup>, P. Perrod<sup>11</sup>, S. Peters<sup>9</sup>, P. Pharabod<sup>11</sup>, W. Pirm<sup>9</sup>, K. Rauschnabel<sup>3</sup>, A. Reboux<sup>10</sup>, P. Reimer<sup>3</sup>, P. Ribarics<sup>9</sup>, M. Rie<sup>12</sup>, M. Rudowicz<sup>3</sup>, S. Rusaakov<sup>5</sup>, V. Rusinov<sup>7</sup>, K. Rybicki<sup>3</sup>, N. Sahlmann<sup>1</sup>, M. Savitsky<sup>5</sup>, P. Sawal<sup>12</sup>, P. Schacht<sup>9</sup>, W. Schmitz<sup>7</sup>, H. Schmücker<sup>9</sup>, M. Seman<sup>6</sup>, V. Shelkalyan<sup>7</sup>, I. Sheviakov<sup>8</sup>, Y. Siro<sup>12</sup>, K. Thiele<sup>5</sup>, I. Tichomirov<sup>7</sup>, W. Tribanek<sup>2</sup>, P. Staroba<sup>13</sup>, P. Štefan<sup>7</sup>, H. Steiner<sup>12</sup>, J. Stier<sup>5</sup>, J. Stracho<sup>12</sup>, M. Urban<sup>11</sup>, S. Valkar<sup>14</sup>, A. Valkarova<sup>14</sup>, C. Vallée<sup>12</sup>, M. Vecko<sup>13</sup>, P. Verrecchia<sup>4</sup>, G. Vill<sup>12</sup>, D. Wegener<sup>3</sup>, P. Weissbach<sup>9</sup>, H.-P. Wellisch<sup>9</sup>, T. P. Yiou<sup>12</sup>, J. Žáček<sup>10,14</sup>, P. Závada<sup>13</sup>, Ch. Zeit<sup>12</sup>, F. Zomer<sup>10</sup>

<sup>1</sup> III. Physikalisches Institut der RWTH, Aachen, Germany <sup>a</sup>

<sup>2</sup> Institute for Nuclear Physics, Cracow, Poland <sup>b</sup>

<sup>3</sup> Institut für Physik, Universität Dortmund, Dortmund, Germany <sup>a</sup>

<sup>4</sup> DAPNIA, Centre d'Etudes de Saclay, Gif-sur-Yvette, France

<sup>5</sup> DESY, Hamburg, Germany

<sup>6</sup> Institute of Experimental Physics, Slovak Academy of Sciences, Košice, Slovakia

<sup>7</sup> Institute for Theoretical and Experimental Physics, Moscow, Russia

<sup>8</sup> Lebedev Physical Institute, Moscow, Russia

<sup>9</sup> Max-Planck-Institut für Physik, München, Germany <sup>a</sup>

<sup>10</sup> LAL, Université Paris-Sud, IN2P3-CNRS, Orsay, France

<sup>11</sup> LPNHE, Ecole Polytechnique, IN2P3-CNRS, Palaiseau, France

<sup>12</sup> LPNHE, Universités Paris VI and VII, IN2P3-CNRS, Paris, France

<sup>13</sup> Institute of Physics, Czech Academy of Sciences, Praha, Czech Republic

<sup>14</sup> Nuclear Center, Charles University, Praha, Czech Republic

<sup>†</sup> Deceased

<sup>a</sup> Supported by the Bundesministerium für Forschung und Technologie, FRG, under contract numbers 6AC17P, 6AC17P, 6DO87I, and 6MP17I

<sup>b</sup> Supported by the Polish State Committee for Scientific Research, grant No. 204209101

## 1 Introduction

The electron proton collider HERA has recently come into operation at DESY(Hamburg). The experimental program extends the tests of the standard model to regions of high momentum transfer  $Q^2 (\leq 4 * 10^4 \text{ GeV}^2)$  and low Bjorken  $x (\sim 10^{-4})$ . It also puts emphasis on search for new physics, such as supersymmetric particles,leptoquarks, lepton and quark substructures, new bosons, heavy leptons. The H1 detector has been designed to match these goals, by providing an excellent identification and precise measurement of electrons, muons and penetrating neutral particles, combined with very good performances in the inclusive measurement of neutral and charged current interactions [1] - [5].

The general structure of the H1 detector can be seen in Figs. 1 and 2 which show two cuts parallel and perpendicular to the beams respectively. The main elements of the detector are a compact tracking detector surrounded by an electromagnetic (e.m.) and hadronic liquid argon calorimeter covering most of the angular range, both being positioned inside a large superconducting solenoid, with the magnetic field parallel to the beam direction. The iron yoke is instrumented and is used as a tail catcher for hadronic showers, and as an additional filter for muons detected in several layers of planar chambers covering the barrel and forward regions of the detector.

This paper describes the liquid argon calorimeter which is so far the largest ever built and located inside a large superconducting coil in a separate cryostat. Thirteen laboratories have participated in the construction. For many of the components, original solutions had to be found and developed, and will be detailed in the course of the paper. The main achievements can be summarised as follows:

- The large cryostat and the cryogenic system have been operated very smoothly and in a satisfactory way since the cool down in January 1991.
- The argon quality is continuously monitored, its purity is found to be high and stable to better than 0.5 % per year.
- The entire calorimeter is hermetically closed. Both the e.m. and hadronic stacks are contiguously connected without dead material between them. For the hadronic stacks, independent read-out cells ensure the precision of the charge measurement.
- The electronic read-out chain is very stable at the level of 0.2 %, and needs to be calibrated only once every few weeks.
- The data acquisition system employs Digital Signal Processors (DSP) after the signal digitization. It allows the powerful and fast data reduction which is necessary for the high number of channels (45000) and the high trigger rate of H1 (1 kHz).
- Finally, a very sophisticated first level trigger has been built for the first time with a liquid argon calorimeter without any dead time and allowing minimal energy cuts as low as 2 GeV. This trigger will allow the selection of physics events, while the tracker trigger will be used essentially for removing the background.
- Each type of calorimeter module has been extensively tested and calibrated in a test beam at CERN. Runs with cosmic rays have also been performed with the full calorimeter at

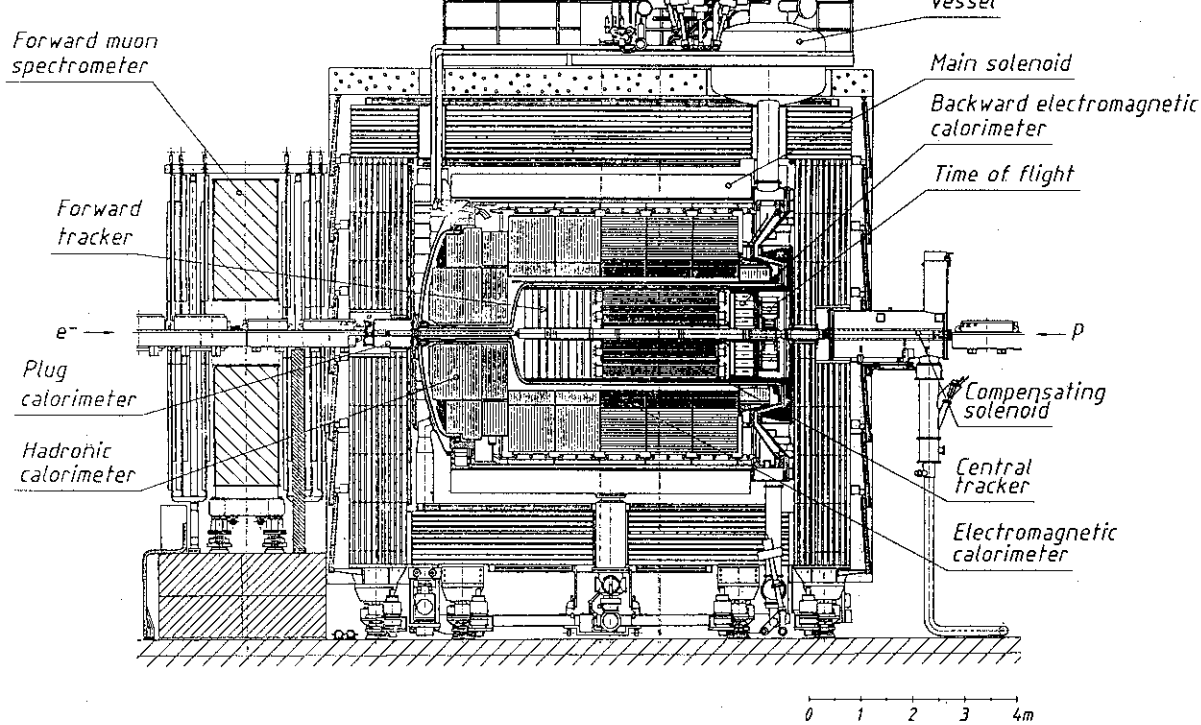


Figure 1: Longitudinal cross section of the H1 detector.

DESY. The main results are presented at the end of the paper and will be discussed in more detail in subsequent publications.

## 2 Physics Requirements

The properties required for the calorimeter have been quantitatively estimated [1] in order to allow precise measurements of the structure functions [6, 7]. The liquid argon technique has been chosen in order to ensure a good stability and an easy calibration, a homogeneous response and the possibility of a fine granularity. Besides a very good hermeticity and a good homogeneity, the requirements in the two parts of the calorimeter are the following:

In the electromagnetic part:

- The resolution for electrons should be  $\sigma(E)/E \sim 0.10/\sqrt{E}$ .
- The stability of the response has to be at the 1% level
- In order to get precise angular reconstruction and to ensure a good  $e/\pi$  rejection ( $< 10^{-3}$ ) the read-out structure must have a fine transversal and longitudinal segmentation (later dimensions of the pads of the order of the Molière radius  $r_M$  and at least 3 longitudinal segments everywhere).
- The electromagnetic showers should be fully contained.

In the hadronic part:

- The resolution for hadrons should be  $\sigma(E)/E \sim 0.55/\sqrt{E}$ .
- The overall stability has to be  $\sim 2\%$ .
- The hadronic showers cannot be fully contained in the calorimeter at high energy, they have to be when adding the energy seen in the tail catcher calorimeter.

These requirements put constraints on the design of the calorimeter. In order to provide hermeticity and homogeneity, dead materials and cracks have to be minimized. The calorimeter should cover most of the solid angle in a single cryostat (Figs. 3 and 4). Nevertheless, the insertion of the tracker components imposes a free space for a polar angle  $\theta > 154^\circ$ , which is closed by a lead / scintillator calorimeter. This leaves only the backward beam hole uncovered ( $\theta > 174^\circ$ ); the forward beam hole ( $\theta < 4^\circ$ ) is partly covered by the plug calorimeter.

The absorber material in the electromagnetic part is lead. The required energy resolution leads to a plate thickness of 2.4 mm, the total thickness varies between 20 and 30 radiation lengths ( $X_0$ ) (Fig. 4). The absorber material in the hadronic part consists of 16 mm thick stainless steel plates with additional 3 mm steel in the read-out elements. Since the electron response is different from the hadron response in a lead / steel calorimeter with liquid argon as read-out medium, the required resolution is obtained by off-line weighting methods making use of the large difference in the development of the electromagnetic and hadronic components of hadronic showers. These methods put constraints on the longitudinal segmentation of the hadronic part.

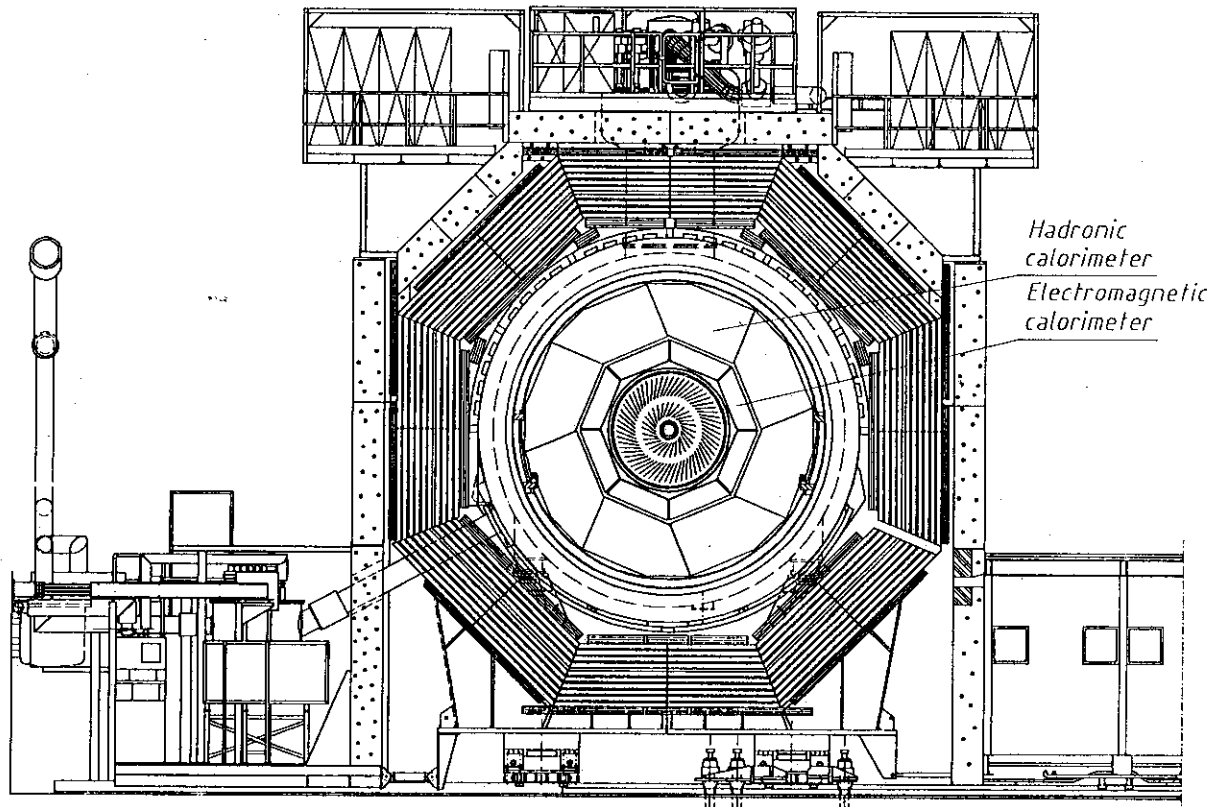


Figure 2: Transversal cross section of the H1 detector (in electron direction).

0 1 2 3 4m

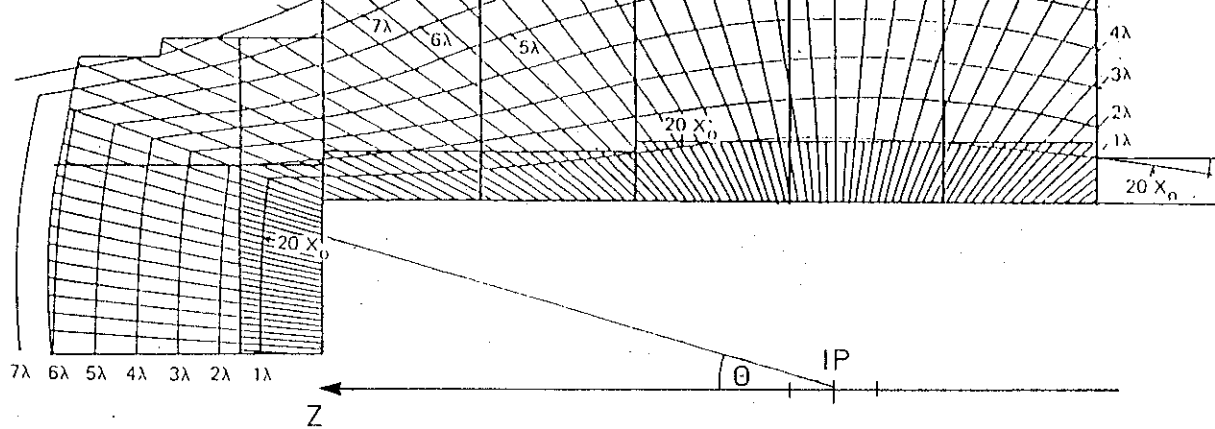


Figure 4: Lines of constant  $\lambda_{obs}$  and  $X_0$  in the liquid argon calorimeter along a cut in the azimuthal midplane of an octant.

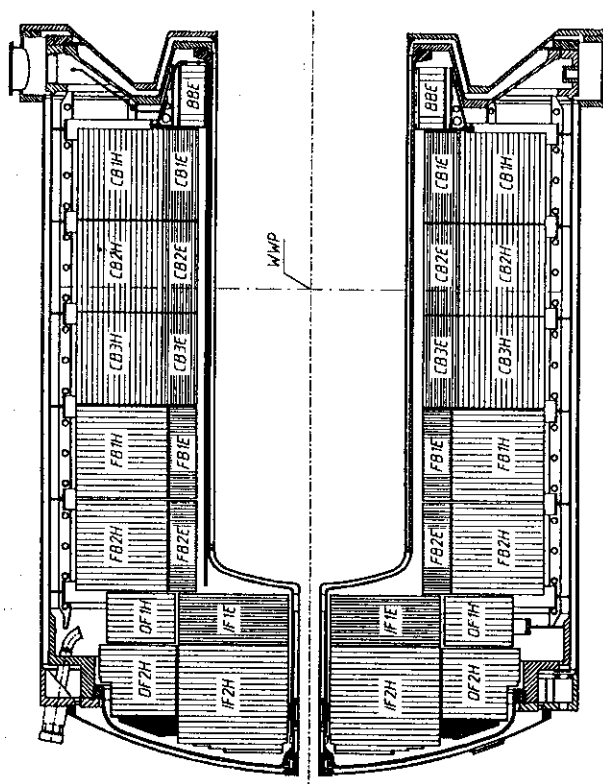


Figure 3: Longitudinal cross section of the H1 liquid argon calorimeter. The orientation of absorber plates is indicated by horizontal and vertical lines respectively.

of the calorimeter: Each tower segment must have a depth of  $\sim 1$  interaction length ( $\lambda_{ab}$ ). The total amount of absorbing material varies between  $4.5$  and  $8 \lambda_{ab}$ , as shown in Fig. 4.

The argon gaps are  $2.35$  mm in the electromagnetic and twice  $2.4$  mm in the hadronic part. In order to keep the systematic errors at the required level, the total argon thickness has to be constant within  $\sim 1\%$  in the electromagnetic and within  $\sim 2\%$  in the hadronic part. This requires a precision of the individual argon gaps of  $50 \mu\text{m}$  in the electromagnetic and of  $100 \mu\text{m}$  in the hadronic part. For absorber plates the variation in thickness has to be  $< 40 \mu\text{m}$  for lead and  $< 400 \mu\text{m}$  for steel.

The last building constraint due to physics is linked to the calorimeter trigger, for which the collected energies must belong to a unique bunch crossing  $t_0$  of the accelerator. This trigger is built from sums of neighbouring segments. It is required that the capacities of these segments are equal to  $\pm 5\%$  in order to allow for an accurate determination of the bunch crossing time  $t_0$ .

### 3 Cryostat and Cryogenic System

This section deals with the cryogenic liquid argon system that consists of:

- a single cryostat with vacuum insulation containing the calorimeter modules and the liquid argon,
- the storage dewars, transfer lines, controls and safety devices required for stable operation as well as for cooling down and warming up.

A short summary of the cryogenic operations since 1991 is given at the end of this chapter.

#### 3.1 Cryostat

The main design requirements for this vessel were to maximize the space available for calorimeter modules as well as to minimize the wall thickness in front of the electromagnetic calorimeter and between the hadronic calorimeter and the iron. Furthermore, the vessel should withstand a maximum pressure of 3 bars and support the total load of the calorimeter modules ( $\sim 500$  t).

The cryostat is a cylindrical dewar consisting of two shells separated by vacuum insulation and superinsulation material. Figure 5 shows the overall layout and Tab. 1 lists the main characteristics of this cryostat. All walls are made of stainless steel except for the inner wall of the vacuum vessel, around the beam-pipe and the central tracker, which is made of aluminium alloy. A series of longitudinal spars and circular ribs on the inner part of the cold vessel contribute to the mechanical stiffness of the vessel and allow the integration of the stack support system.

The total amount of material in front of the calorimeter is displayed in Fig. 6.

The inner vessel front and rear walls are welded to the main inner cylindrical vessel. A special bimetal (S.S./Al) junction at the front end of the inner cold tube, together with a bellow welded to the stainless steel part, allows to take up the difference in thermal expansion between the outer stainless steel walls and the inner aluminium one ( $1 \text{ mm/m}$  for  $\Delta T \sim 200 \text{ K}$ ). At the rear a double elastic joint is used.

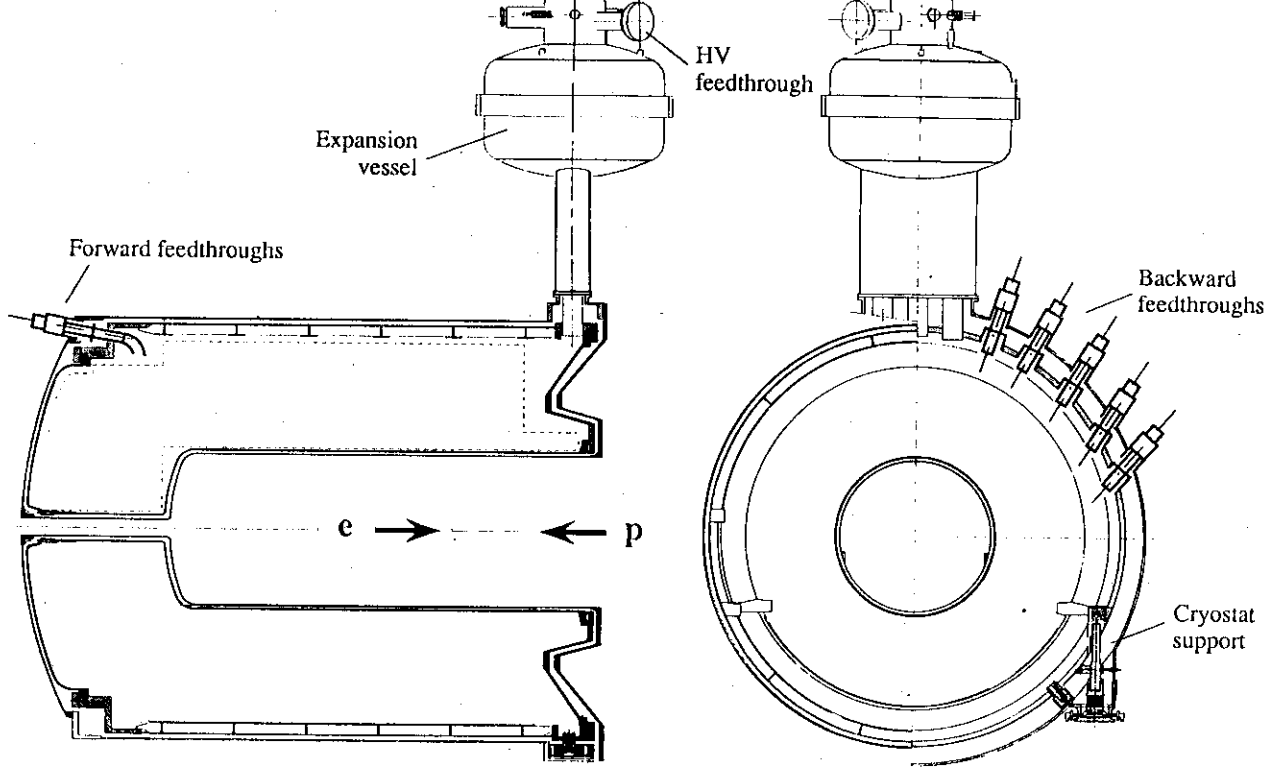


Figure 5 : Longitudinal and transversal cut of H1 cryostat

<b>Vacuum vessel</b>	5.15 m 1.82 m 0.20 m 7.15 m 20 mm 8 mm 8 mm 8 mm 15 mm 25-70 mm 41 t 120 m <sup>3</sup> 1.9 t 20 m <sup>3</sup>
<b>Liquid argon vessel</b>	5.00 m 1.91 m 0.33 m 6.95 m 9.40 m 15 mm 20 mm 14 mm 12 mm 20 mm 30-100 mm 15 t 100 m <sup>3</sup> 53 m <sup>3</sup> 1.9 t 1.35 bar 1.0 bar 600 t

Table 1: Main characteristics of the liquid argon cryostat.

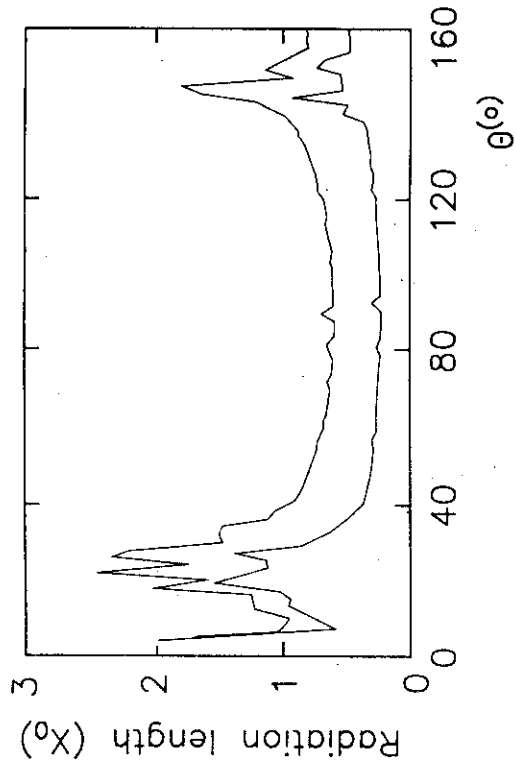


Figure 6: Amount of dead material ( $X_0$ ) in front of the calorimeter vs. the polar angle  $\theta$ . The lower (upper) curve shows the material due to the tracker (tracker + cryostat).

The weight of the full cold vessel (~600 t including the calorimeters and ~80 t of liquid argon is transferred directly down through the cryostat walls to the central iron yoke. These forces are taken through the insulating vacuum on four feet of low thermal conductivity made of flint glass and located between the end flange of the magnet cryostat and the muon chambers. The feet stand on warm teflon-coated sliding surfaces thus allowing for the differential displacements occurring during cool-down and warm-up.

An expansion vessel (4.7 m<sup>3</sup>) located at the rear of the cryostat and partly covered by the iron yoke, is directly connected to the cold vessel through a chimney with no valves to avoid accidental shutting off of this relief volume. This chimney also houses the argon and nitrogen lines needed for the cryogenic operation as well as the high voltage (HV) cables of the calorimeter. The liquid nitrogen for the main cooling coils is fed in at the front part of the cryostat, whereas a port located at the bottom of the rear part of the cryostat is used in the circulation scheme for cooling down by injection of cold helium and for filling or emptying of the liquid argon. 3072 flat cables of 16 channels each are brought out of the cryostat through 24 special tubular ports distributed at both ends around the top half of the vessel. Figure 7 shows the principle of such feed-throughs. The cables within these tubes are packed within a thermal insulation forming a heat-exchanger and preventing convection currents within the tube. Note that there is no flow of argon in the feed-throughs.

The 1504 HV cables exit from the cryostat through the top of the expansion vessel by a specially developed single feed-through.

Overall heat losses (stable conditions)	3.8 kW
Corresponding LN <sub>2</sub> flow	95 l/h
Heat losses due to cables	1.2 kW
Cool-down time	29 days
Total quantity of LN <sub>2</sub> for cool-down	190 m <sup>3</sup>
Time to fill up cryostat	5 hours
Time to empty cryostat	2.5 hours
Regulation pressure	1.35 ± 0.05 bar (Abs)
Operating temperature	90.2 ± 0.1 K

Table 2: Parameters of the cryogenic system.

### 3.2 Cryogenics

The layout of the cryogenic system is shown in Fig. 8, its main parameters are listed in Table 2. Refrigeration for the cool-down, stable operation and argon storage dewar is provided by liquid nitrogen supplied from a 25000 l storage dewar filled by a liquid nitrogen liquefier or an external supply.

The cryogenic system was designed to allow a maximum cool-down time of 29 days, transfer of liquid argon into the cold cryostat in less than 5 hours, transfer of liquid argon out of the cryostat in less than 2.5 hours and a maximum warm-up time of 30 days. Cooling down liquid argon temperature is achieved by circulation of helium gas cooled in an external movable liquid nitrogen heat exchanger. Stable operation is ensured by a regulated flow liquid nitrogen through three sets of coils, the main one located along the top half of the vessel, another one located around the bubble shield which is on the top half of the larger part of the inner cold wall, and the third one in the expansion vessel.

Complete control of all processes is done by a system of VME processors with an OS9 operating system coupled to a GRAFCET control process [8]. This enables all operations including cool-down / warm-up and filling / emptying to be automatically done under computer control.

The complete calorimeter was effectively cooled down in 25 days in early 1991 and has remained cold since then. The average liquid nitrogen consumption was 600 l/h during the cool-down and ~95 l/h during stable operation. 250 m<sup>3</sup> of helium gas and 190 m<sup>3</sup> of liquid nitrogen were needed for the whole cool-down process. The time needed for filling with liquid argon was ~2.5 h.

The pressure in the gaseous part of the expansion vessel was regulated to 1.35 ± 0.05 bar enabling the temperature of the liquid argon to be kept at a stable value of 90.2 ± 0.1 K.

When moving into the beam in early 1992, the cold vessel was emptied to comply with local safety rules and the cooling lines were disconnected, effectively stopping the cooling for ten days. During this period the average cryostat temperature rose by about 15 degrees, from a bottom to top temperature gradient of 30 degrees on the cryostat walls and 25 degrees on the calorimeter modules. Refilling was done within 5 hours after a one day cool-down to bring the calorimeter to ~100 K.

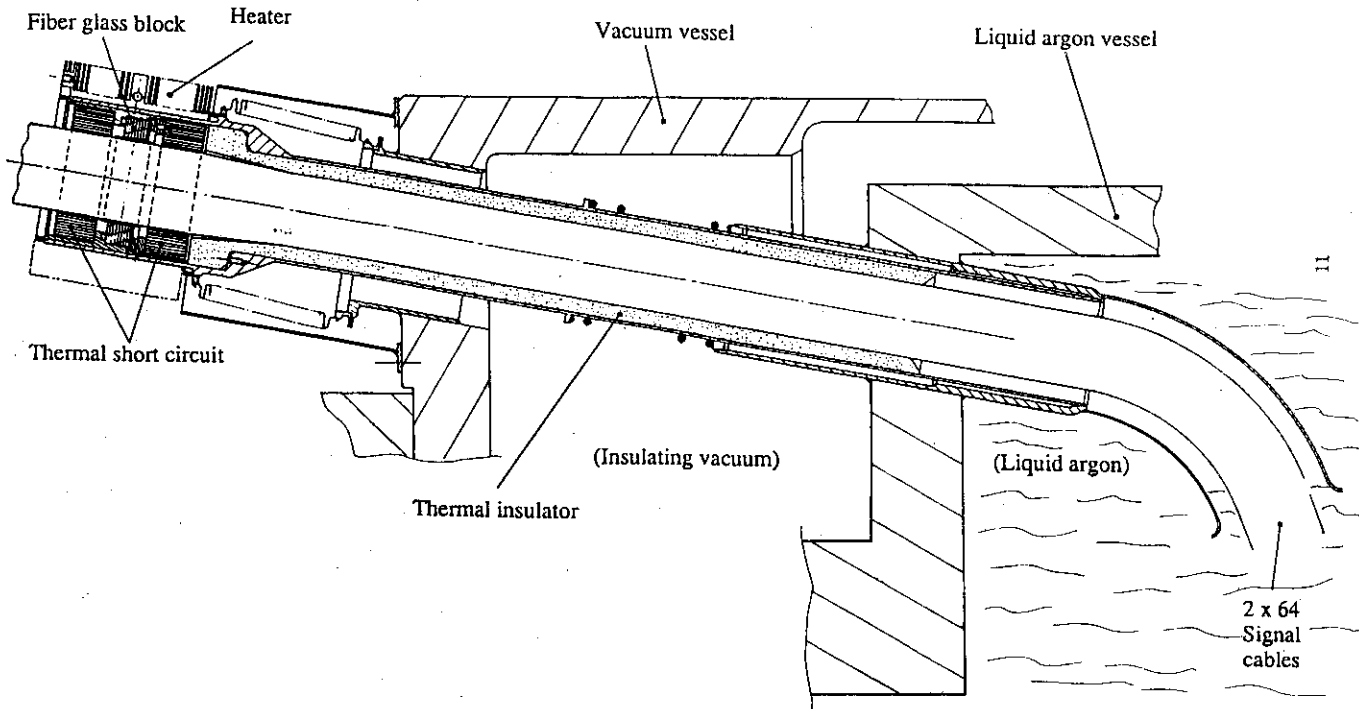


Figure 7: Schematic of the feed-through for signal cables.

### 3.3 Liquid argon purity measurements

A system monitoring the liquid argon purity is integrated into the H1 liquid argon calorimeter to check the stability of the ratio of energy loss to collected charge at the required level of  $\ll$ . The goal is to monitor any variation of this ratio as a function of time and its dependence on the location inside the cryostat.

The basic sensor is a liquid argon ionization chamber with a nominal electrical field of 1 kV/cm. Its cathode is coated with a  $^{207}\text{Bi}$  source with an activity of  $10^4$  Bq. Each purity probe is in a chamber equipped with an independent HV supply, a low noise charge sensitive preamplifier working in the cold [9] and a calibration input through a 10 pF capacitor. An amplification and multiplexing stage located outside of the cryostat output signals are sent to a spectroscopy amplifier. The energy spectra of the radioactive decays are accumulated for probe successively. An on-line shape analysis yields the average pulse heights corresponding either to the 481 keV conversion-electron peak or to the upper edge of the spectrum around 1050 keV. The latter measurement is the most precise ( $\sim 0.3\%$ ) because it does not suffer from the Compton background. It is not affected by the dispersion of the center of gravity of the ionization blob inside the liquid argon gap. The specific charge distribution in the active volume yields the factor relating the attenuations of the charge collection due to a given electron free path in the probe and in a calorimeter stack. For example a typical probe is 3.4 times more sensitive to impurities than the calorimeter. Using this factor during the CERN calibration runs, the effects due to changes of the liquid argon purity on the electron beam signals can be successfully related to the  $^{207}\text{Bi}$  signals. Hence all purity measurements can be conveniently expressed in the same "H1 purity unit" (fraction of charge collected from an electromagnetic shower by the H1 calorimeter at the nominal electric field).

The complete purity monitoring system consists of ten probes distributed in the H1 cryostat plus one in a small movable cryostat for testing liquid argon samples and six in the CERN calibration cryostat. At delivery, or after each filling, the purity of the liquid argon is evaluated by fitting the "HV curve" as in ref. [10], i.e. charge collection efficiency versus electrical field. Then the relative variations of purity are monitored continuously for each probe as shown in Fig. 9. The operations are fully automated by a PC connected to the OS9 computer in charge of slow controls. An off-line analysis is done in order to control systematic errors at the design level of 0.1%.

The results of nearly two years of operation show that cumulative effects of the liquid argon pollution are well below our 1% goal. During the CERN calibration runs (see below), we have observed different levels of degradation of the argon purity with time for different calorimeter stacks [11]. We attribute this to the fact that the flushing and cool-down procedure was different from the one used finally at H1.

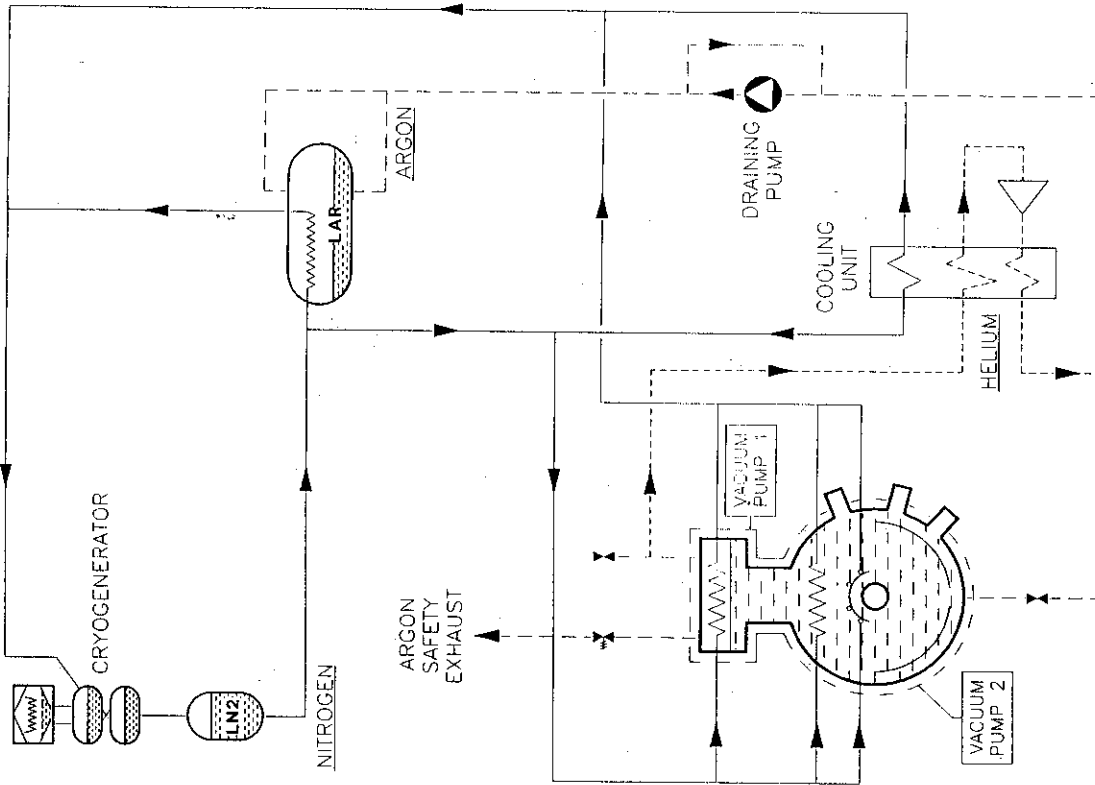


Figure 8: Layout of the cryogenic system.

## 4 Stack Design and Construction

### 4.1 General layout

The physics requirements and the general characteristics of the calorimeter have been given in section 2. The segmentation of the liquid argon calorimeter in stacks is the result of a compromise between the minimization of dead volumes (cracks) and the practical feasibility and handling. In the beam (z) direction the calorimeter is segmented into 8 wheels (Fig. 9). Their structure is self-supporting. Throughout the calorimeter we have chosen an eight  $\varphi$ -segmentation with pointing cracks in the electromagnetic and strongly non-pointing cracks in the hadronic section (Fig. 10). A good containment is kept in this way and the energy deposited around the crack region can be corrected for at the event-by-event basis.

The orientation of the absorber plates (Fig. 3) was chosen such that the angle of incidence is not smaller than  $45^\circ$ . Therefore the orientation of the absorber plates is vertical in the forward and backward, and parallel to the beam in the central region. In the electromagnetic part, lead plates are mechanically stabilized by fiberglass(G10) plates glued to them. The thickness of the liquid argon gap is defined by spacers. This technique cannot be extrapolated to much thicker and larger plates in the hadronic section. Therefore we have used stainless steel as absorber in the hadronic section. The tolerances on thickness and flatness of the 16 thick and up to 2.5 m long plates do not allow to define the gap thickness with the precision necessary. Hence a sensing structure independent of the absorber plates is used to define the liquid argon gap. These read-out cells are inserted into the gap between the absorber plates. The nominal design parameters of the different calorimeter stacks are collected in Tab. 3, 4, 5, 6, 7, 8, 9, 10, 11, 12, 13, 14, 15, 16, 17, 18, 19, 20, 21, 22, 23, 24, 25, 26, 27, 28, 29, 30, 31, 32, 33, 34, 35, 36, 37, 38, 39, 40, 41, 42, 43, 44, 45, 46, 47, 48, 49, 50, 51, 52, 53, 54, 55, 56, 57, 58, 59, 60, 61, 62, 63, 64, 65, 66, 67, 68, 69, 70, 71, 72, 73, 74, 75, 76, 77, 78, 79, 80, 81, 82, 83, 84, 85, 86, 87, 88, 89, 90, 91, 92, 93, 94, 95, 96, 97, 98, 99, 100, 101, 102, 103, 104, 105, 106, 107, 108, 109, 110, 111, 112, 113, 114, 115, 116, 117, 118, 119, 120, 121, 122, 123, 124, 125, 126, 127, 128, 129, 130, 131, 132, 133, 134, 135, 136, 137, 138, 139, 140, 141, 142, 143, 144, 145, 146, 147, 148, 149, 150, 151, 152, 153, 154, 155, 156, 157, 158, 159, 160, 161, 162, 163, 164, 165, 166, 167, 168, 169, 170, 171, 172, 173, 174, 175, 176, 177, 178, 179, 180, 181, 182, 183, 184, 185, 186, 187, 188, 189, 190, 191, 192, 193, 194, 195, 196, 197, 198, 199, 200, 201, 202, 203, 204, 205, 206, 207, 208, 209, 210, 211, 212, 213, 214, 215, 216, 217, 218, 219, 220, 221, 222, 223, 224, 225, 226, 227, 228, 229, 230, 231, 232, 233, 234, 235, 236, 237, 238, 239, 240, 241, 242, 243, 244, 245, 246, 247, 248, 249, 250, 251, 252, 253, 254, 255, 256, 257, 258, 259, 260, 261, 262, 263, 264, 265, 266, 267, 268, 269, 270, 271, 272, 273, 274, 275, 276, 277, 278, 279, 280, 281, 282, 283, 284, 285, 286, 287, 288, 289, 290, 291, 292, 293, 294, 295, 296, 297, 298, 299, 300, 301, 302, 303, 304, 305, 306, 307, 308, 309, 310, 311, 312, 313, 314, 315, 316, 317, 318, 319, 320, 321, 322, 323, 324, 325, 326, 327, 328, 329, 330, 331, 332, 333, 334, 335, 336, 337, 338, 339, 340, 341, 342, 343, 344, 345, 346, 347, 348, 349, 350, 351, 352, 353, 354, 355, 356, 357, 358, 359, 360, 361, 362, 363, 364, 365, 366, 367, 368, 369, 370, 371, 372, 373, 374, 375, 376, 377, 378, 379, 380, 381, 382, 383, 384, 385, 386, 387, 388, 389, 390, 391, 392, 393, 394, 395, 396, 397, 398, 399, 400, 401, 402, 403, 404, 405, 406, 407, 408, 409, 410, 411, 412, 413, 414, 415, 416, 417, 418, 419, 420, 421, 422, 423, 424, 425, 426, 427, 428, 429, 430, 431, 432, 433, 434, 435, 436, 437, 438, 439, 440, 441, 442, 443, 444, 445, 446, 447, 448, 449, 450, 451, 452, 453, 454, 455, 456, 457, 458, 459, 460, 461, 462, 463, 464, 465, 466, 467, 468, 469, 470, 471, 472, 473, 474, 475, 476, 477, 478, 479, 480, 481, 482, 483, 484, 485, 486, 487, 488, 489, 490, 491, 492, 493, 494, 495, 496, 497, 498, 499, 500, 501, 502, 503, 504, 505, 506, 507, 508, 509, 510, 511, 512, 513, 514, 515, 516, 517, 518, 519, 520, 521, 522, 523, 524, 525, 526, 527, 528, 529, 530, 531, 532, 533, 534, 535, 536, 537, 538, 539, 540, 541, 542, 543, 544, 545, 546, 547, 548, 549, 550, 551, 552, 553, 554, 555, 556, 557, 558, 559, 560, 561, 562, 563, 564, 565, 566, 567, 568, 569, 570, 571, 572, 573, 574, 575, 576, 577, 578, 579, 580, 581, 582, 583, 584, 585, 586, 587, 588, 589, 590, 591, 592, 593, 594, 595, 596, 597, 598, 599, 600, 601, 602, 603, 604, 605, 606, 607, 608, 609, 610, 611, 612, 613, 614, 615, 616, 617, 618, 619, 620, 621, 622, 623, 624, 625, 626, 627, 628, 629, 630, 631, 632, 633, 634, 635, 636, 637, 638, 639, 640, 641, 642, 643, 644, 645, 646, 647, 648, 649, 650, 651, 652, 653, 654, 655, 656, 657, 658, 659, 660, 661, 662, 663, 664, 665, 666, 667, 668, 669, 670, 671, 672, 673, 674, 675, 676, 677, 678, 679, 680, 681, 682, 683, 684, 685, 686, 687, 688, 689, 690, 691, 692, 693, 694, 695, 696, 697, 698, 699, 700, 701, 702, 703, 704, 705, 706, 707, 708, 709, 710, 711, 712, 713, 714, 715, 716, 717, 718, 719, 720, 721, 722, 723, 724, 725, 726, 727, 728, 729, 730, 731, 732, 733, 734, 735, 736, 737, 738, 739, 740, 741, 742, 743, 744, 745, 746, 747, 748, 749, 750, 751, 752, 753, 754, 755, 756, 757, 758, 759, 760, 761, 762, 763, 764, 765, 766, 767, 768, 769, 770, 771, 772, 773, 774, 775, 776, 777, 778, 779, 780, 781, 782, 783, 784, 785, 786, 787, 788, 789, 790, 791, 792, 793, 794, 795, 796, 797, 798, 799, 800, 801, 802, 803, 804, 805, 806, 807, 808, 809, 810, 811, 812, 813, 814, 815, 816, 817, 818, 819, 820, 821, 822, 823, 824, 825, 826, 827, 828, 829, 830, 831, 832, 833, 834, 835, 836, 837, 838, 839, 840, 841, 842, 843, 844, 845, 846, 847, 848, 849, 850, 851, 852, 853, 854, 855, 856, 857, 858, 859, 860, 861, 862, 863, 864, 865, 866, 867, 868, 869, 870, 871, 872, 873, 874, 875, 876, 877, 878, 879, 880, 881, 882, 883, 884, 885, 886, 887, 888, 889, 890, 891, 892, 893, 894, 895, 896, 897, 898, 899, 900, 901, 902, 903, 904, 905, 906, 907, 908, 909, 910, 911, 912, 913, 914, 915, 916, 917, 918, 919, 920, 921, 922, 923, 924, 925, 926, 927, 928, 929, 930, 931, 932, 933, 934, 935, 936, 937, 938, 939, 940, 941, 942, 943, 944, 945, 946, 947, 948, 949, 950, 951, 952, 953, 954, 955, 956, 957, 958, 959, 960, 961, 962, 963, 964, 965, 966, 967, 968, 969, 970, 971, 972, 973, 974, 975, 976, 977, 978, 979, 980, 981, 982, 983, 984, 985, 986, 987, 988, 989, 990, 991, 992, 993, 994, 995, 996, 997, 998, 999, 1000, 1001, 1002, 1003, 1004, 1005, 1006, 1007, 1008, 1009, 1010, 1011, 1012, 1013, 1014, 1015, 1016, 1017, 1018, 1019, 1020, 1021, 1022, 1023, 1024, 1025, 1026, 1027, 1028, 1029, 1030, 1031, 1032, 1033, 1034, 1035, 1036, 1037, 1038, 1039, 1040, 1041, 1042, 1043, 1044, 1045, 1046, 1047, 1048, 1049, 1050, 1051, 1052, 1053, 1054, 1055, 1056, 1057, 1058, 1059, 1060, 1061, 1062, 1063, 1064, 1065, 1066, 1067, 1068, 1069, 1070, 1071, 1072, 1073, 1074, 1075, 1076, 1077, 1078, 1079, 1080, 1081, 1082, 1083, 1084, 1085, 1086, 1087, 1088, 1089, 1090, 1091, 1092, 1093, 1094, 1095, 1096, 1097, 1098, 1099, 1100, 1101, 1102, 1103, 1104, 1105, 1106, 1107, 1108, 1109, 1110, 1111, 1112, 1113, 1114, 1115, 1116, 1117, 1118, 1119, 1120, 1121, 1122, 1123, 1124, 1125, 1126, 1127, 1128, 1129, 1130, 1131, 1132, 1133, 1134, 1135, 1136, 1137, 1138, 1139, 1140, 1141, 1142, 1143, 1144, 1145, 1146, 1147, 1148, 1149, 1150, 1151, 1152, 1153, 1154, 1155, 1156, 1157, 1158, 1159, 1160, 1161, 1162, 1163, 1164, 1165, 1166, 1167, 1168, 1169, 1170, 1171, 1172, 1173, 1174, 1175, 1176, 1177, 1178, 1179, 1180, 1181, 1182, 1183, 1184, 1185, 1186, 1187, 1188, 1189, 1190, 1191, 1192, 1193, 1194, 1195, 1196, 1197, 1198, 1199, 1200, 1201, 1202, 1203, 1204, 1205, 1206, 1207, 1208, 1209, 1210, 1211, 1212, 1213, 1214, 1215, 1216, 1217, 1218, 1219, 1220, 1221, 1222, 1223, 1224, 1225, 1226, 1227, 1228, 1229, 1230, 1231, 1232, 1233, 1234, 1235, 1236, 1237, 1238, 1239, 1240, 1241, 1242, 1243, 1244, 1245, 1246, 1247, 1248, 1249, 1250, 1251, 1252, 1253, 1254, 1255, 1256, 1257, 1258, 1259, 1260, 1261, 1262, 1263, 1264, 1265, 1266, 1267, 1268, 1269, 1270, 1271, 1272, 1273, 1274, 1275, 1276, 1277, 1278, 1279, 1280, 1281, 1282, 1283, 1284, 1285, 1286, 1287, 1288, 1289, 1290, 1291, 1292, 1293, 1294, 1295, 1296, 1297, 1298, 1299, 1300, 1301, 1302, 1303, 1304, 1305, 1306, 1307, 1308, 1309, 1310, 1311, 1312, 1313, 1314, 1315, 1316, 1317, 1318, 1319, 1320, 1321, 1322, 1323, 1324, 1325, 1326, 1327, 1328, 1329, 1330, 1331, 1332, 1333, 1334, 1335, 1336, 1337, 1338, 1339, 1340, 1341, 1342, 1343, 1344, 1345, 1346, 1347, 1348, 1349, 1350, 1351, 1352, 1353, 1354, 1355, 1356, 1357, 1358, 1359, 1360, 1361, 1362, 1363, 1364, 1365, 1366, 1367, 1368, 1369, 1370, 1371, 1372, 1373, 1374, 1375, 1376, 1377, 1378, 1379, 1380, 1381, 1382, 1383, 1384, 1385, 1386, 1387, 1388, 1389, 1390, 1391, 1392, 1393, 1394, 1395, 1396, 1397, 1398, 1399, 1400, 1401, 1402, 1403, 1404, 1405, 1406, 1407, 1408, 1409, 1410, 1411, 1412, 1413, 1414, 1415, 1416, 1417, 1418, 1419, 1420, 1421, 1422, 1423, 1424, 1425, 1426, 1427, 1428, 1429, 1430, 1431, 1432, 1433, 1434, 1435, 1436, 1437, 1438, 1439, 1440, 1441, 1442, 1443, 1444, 1445, 1446, 1447, 1448, 1449, 1450, 1451, 1452, 1453, 1454, 1455, 1456, 1457, 1458, 1459, 1460, 1461, 1462, 1463, 1464, 1465, 1466, 1467, 1468, 1469, 1470, 1471, 1472, 1473, 1474, 1475, 1476, 1477, 1478, 1479, 1480, 1481, 1482, 1483, 1484, 1485, 1486, 1487, 1488, 1489, 1490, 1491, 1492, 1493, 1494, 1495, 1496, 1497, 1498, 1499, 1500, 1501, 1502, 1503, 1504, 1505, 1506, 1507, 1508, 1509, 1510, 1511, 1512, 1513, 1514, 1515, 1516, 1517, 1518, 1519, 1520, 1521, 1522, 1523, 1524, 1525, 1526, 1527, 1528, 1529, 1530, 1531, 1532, 1533, 1534, 1535, 1536, 1537, 1538, 1539, 1540, 1541, 1542, 1543, 1544, 1545, 1546, 1547, 1548, 1549, 1550, 1551, 1552, 1553, 1554, 1555, 1556, 1557, 1558, 1559, 1560, 1561, 1562, 1563, 1564, 1565, 1566, 1567, 1568, 1569, 1570, 1571, 1572, 1573, 1574, 1575, 1576, 1577, 1578, 1579, 1580, 1581, 1582, 1583, 1584, 1585, 1586, 1587, 1588, 1589, 1590, 1591, 1592, 1593, 1594, 1595, 1596, 1597, 1598, 1599, 1600, 1601, 1602, 1603, 1604, 1605, 1606, 1607, 1608, 1609, 1610, 1611, 1612, 1613, 1614, 1615, 1616, 1617, 1618, 1619, 1620, 1621, 1622, 1623, 1624, 1625, 1626, 1627, 1628, 1629, 1630, 1631, 1632, 1633, 1634, 1635, 1636, 1637, 1638, 1639, 1640, 1641, 1642, 1643, 1644, 1645, 1646, 1647, 1648, 1649, 1650, 1651, 1652, 1653, 1654, 1655, 1656, 1657, 1658, 1659, 1660, 1661, 1662, 1663, 1664, 1665, 1666, 1667, 1668, 1669, 1670, 1671, 1672, 1673, 1674, 1675, 1676, 1677, 1678, 1679, 1680, 1681, 1682, 1683, 1684, 1685, 1686, 1687, 1688, 1689, 1690, 1691, 1692, 1693, 1694, 1695, 1696, 1697, 1698, 1699, 1700, 1701, 1702, 1703, 1704, 1705, 1706, 1707, 1708, 1709, 1710, 1711, 1712, 1713, 1714, 1715, 1716, 1717, 1718, 1719, 1720, 1721, 1722, 1723, 1724, 1725, 1726, 1727, 1728, 1729, 1730, 1731, 1732, 1733, 1734, 1735, 1736, 1737, 1738, 1739, 1740, 1741, 1742, 1743, 1744, 1745, 1746, 1747, 1748, 1749, 1750, 1751, 1752, 1753, 1754, 1755, 1756, 1757, 1758, 1759, 1760, 1761, 1762, 1763, 1764, 1765, 1766, 1767, 1768, 1769, 1770, 1771, 1772, 1773, 1774, 1775, 1776, 1777, 1778, 1779, 1780, 1781, 1782, 1783, 1784, 1785, 1786, 1787, 1788, 1789, 1790, 1791, 1792, 1793, 1794, 1795, 1796, 1797, 1798, 1799, 1800, 1801, 1802, 1803, 1804, 1805, 1806, 1807, 1808, 1809, 1810, 1811, 1812, 1813, 1814, 1815, 1816, 1817, 1818, 1819, 1820, 1821, 1822, 1823, 1824, 1825, 1826, 1827, 1828, 1829, 1830, 1831, 1832, 1833, 1834, 1835, 1836, 1837, 1838, 1839, 1840, 1841, 1842, 1843, 1844, 1845, 1846, 1847, 1848, 1849, 1850, 1851, 1852, 1853, 1854, 1855, 1856, 1857, 1858, 1859, 1860, 1861, 1862, 1863, 1864, 1865, 1866, 1867, 1868, 1869, 1870, 1871, 1872, 1873, 1874, 1875, 1876, 1877, 1878, 1879, 1880, 1881, 1882, 1883, 1884, 1885, 1886, 1887, 1888, 1889, 1890, 1891, 1892, 1893, 1894, 1895, 1896, 1897, 1898, 1899, 1900, 1901, 1902, 1903, 1904, 1905, 1906, 1907, 1908, 1909, 1910, 1911, 1912, 1913, 1914, 1915, 1916, 1917, 1918, 1919, 1920, 1921, 1922, 1923, 1924, 1925, 1926, 1927, 1928, 1929, 1930, 1931, 1932, 1933, 1934, 1935, 1936, 1937, 1938, 1939, 1940, 1941, 1942, 1943, 1944, 1945, 1946, 1947, 1948, 1949, 1950, 1951, 1952, 1953, 1954, 1955, 1956, 1957, 1958, 1959, 1960, 1961, 1962, 1963, 1964, 1965, 1966, 1967, 1968, 1969, 1970, 1971, 1972, 1973, 1974, 1975, 1976, 1977, 1978, 1979, 1980, 1981, 1982, 1983, 1984, 1985, 1986, 1987, 1988, 1989, 1990, 1991, 1992, 1993, 1994, 1995, 1996, 1997, 1998, 1999, 2000, 2001, 2002, 2003, 2004, 2005, 2006, 2007, 2008, 2009, 2010, 2011, 2012, 2013, 2014, 2015, 2016, 2017, 2018, 2019, 2020, 2021, 2022, 2023, 2024, 2025, 2026, 2027, 2028, 2029, 2030, 2031, 2032, 2033, 2034, 2035, 2036, 2037, 2038, 2039, 2040, 2041, 2042, 2043, 2044, 2045, 2046, 2047, 2048, 2049, 2050, 2051, 2052, 2053, 2054, 2055, 2056, 2057, 2058, 2059, 2060, 2061, 2062, 2063, 2064, 2065, 2066, 2067, 2068, 2069, 2070, 2071, 2072, 2073, 2074, 2075, 2076, 2077, 2078, 2079, 2080, 2081, 2082, 2083, 2084, 2085, 2086, 2087, 2088, 2089, 2090, 2091, 2092, 2093, 2094, 2095, 2096, 2097, 2098, 2099, 2100, 2101, 2102, 2103, 2104, 2105, 2106, 2107, 2108, 2109, 2110, 2111, 2112, 2113, 2114, 2115, 2116, 2117, 2118, 2119, 2120, 2121, 2122, 2123, 2124, 2125, 2126, 2127, 2128, 2129, 2130, 2131, 2132, 2133, 2134, 2135, 2136, 2137, 2138, 2139, 2140, 2141, 2142, 2143, 2144, 2145, 2146, 2147, 2148, 2149, 2150, 2151, 2152, 2153, 2154, 2155, 2156, 2157, 2158, 2159, 2160, 2161, 2162, 2

- The longitudinal development of a shower should be sampled 3 to 4 times.
- The capacities of those channels which provide a combined input signal to the first-level calorimeter trigger should be equal within  $\pm 5\%$ .
- The overall capacity per electronic channel was chosen to be below 15 nF to limit electronic noise.

In order to meet these conditions, we have chosen a basic granularity of the electromagnetic read-out cells of  $\sim 2 r_M$ 's as measured at the entrance of the electromagnetic calorimeter. For backward electromagnetic part (CB1, CB2, BBE) and for hadronic stacks, the basic dimensions are roughly doubled. The  $\varphi$  - granularity can easily be realized by segmenting the read-plates properly, which realizes also the  $\theta$  - granularity for the stacks with plates parallel to the beam. In the other stacks the  $\theta$  - granularity is achieved by ganging a proper number of consecutive boards. This corresponds to a geometry of read-out towers with projective geometry in  $\varphi$  - and non-projective geometry in  $\theta$  - direction. The overall  $\theta$  - granularity is shown in Fig. 11. The characteristics of the pad structure and the number of electronic channels in different parts of the calorimeter are summarized in Tab. 4 [12].

#### 4.2 Overall mechanics

In the following, the general set up of the stack mechanics common to all wheels is described. The special features of the electromagnetic and hadronic stacks are discussed in detail Sects 4.3 and 4.4.

The eight stacks of a wheel are separated by a narrow gap filled with a minimum amount of material (liquid argon and cables). The insensitive region of a  $\varphi$ -crack corresponds to about 0.5 effective  $r_M$ , hence off-line corrections of the losses in these regions are possible on event-by-event basis (see Sect. 8.4 for further details).

The nominal clearance between two wheels in z-direction amounts to 10 mm with additional space between the wheels FB1/FB2 and FB2/OF available for cables. Independent read-out cells are inserted in the z-cracks in front of the stacks with vertical plates to keep the sample ratio in the crack region between two stacks stable.

Stainless steel of grade 304L was chosen as the absorber material for the hadronic stacks. It is the cheapest steel satisfying the design criteria of low permeability at liquid argon temperature ( $\mu \leq 1.02$ ) and allowing easy welding. Note also that the resistivity is large, hence the forces in case of a quench of the superconducting solenoid are manageable. The basic cell of the hadronic stack is nominally 28 mm thick and consists of a 16 mm thick absorber plate followed by a gap of 12 mm. Independent read-out boards are inserted into the gap like books into a shelf. This configuration is repetitive. Each of the absorber plates must be enclosed between parallel planes of 18 mm thus ensuring the clearance for the independent read-out boards.

The absorber plates are assembled to form a rigid structure by bars perpendicular to the plates and welded to each plate. Each hadronic stack is self-supporting. Eight stacks are located together to form a wheel which has a self-supporting structure. Local reinforcements in region of the locks are necessary. The welding of the plates leaves the  $\varphi$ -crack free of dead material. The forward part of the calorimeter (IF in Fig. 3) is only divided into two half-rim

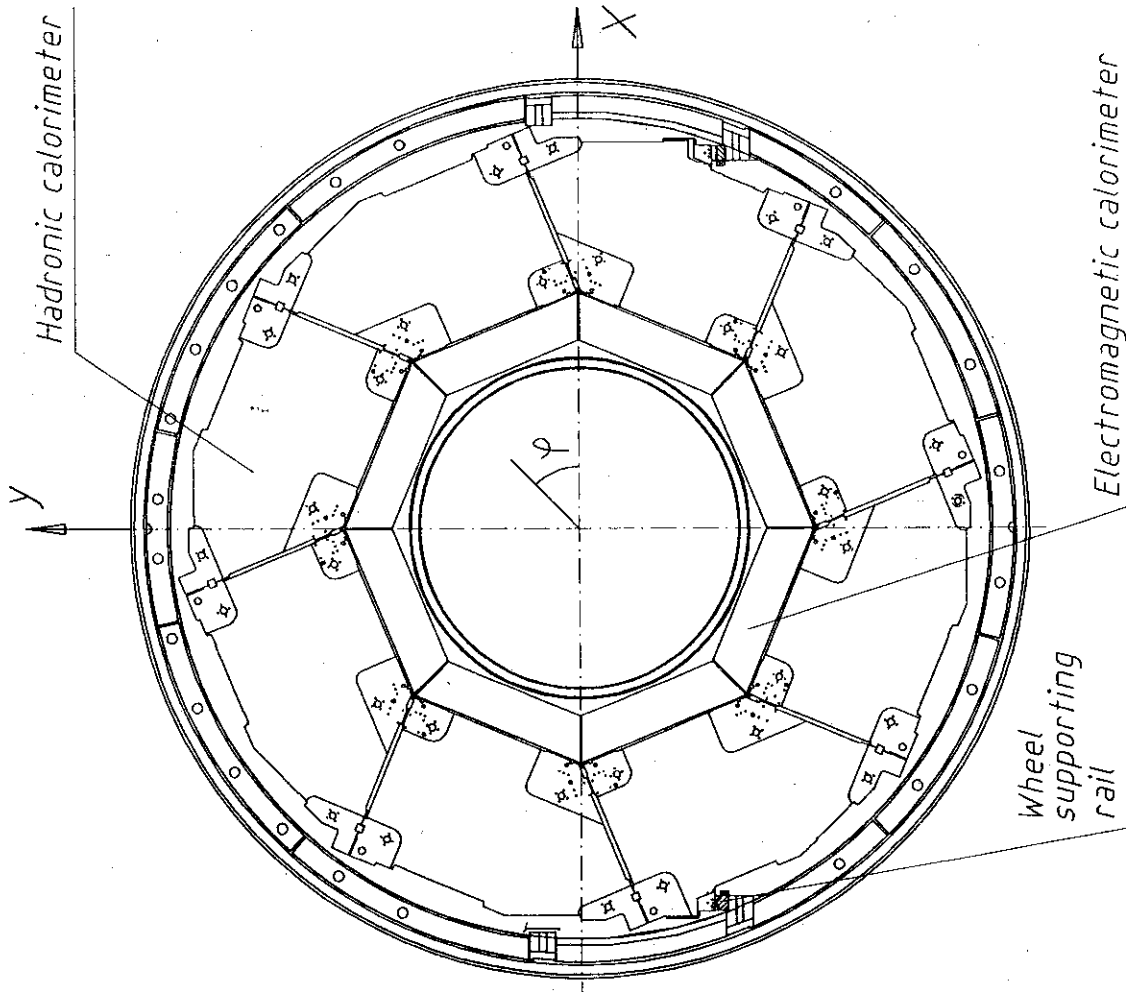
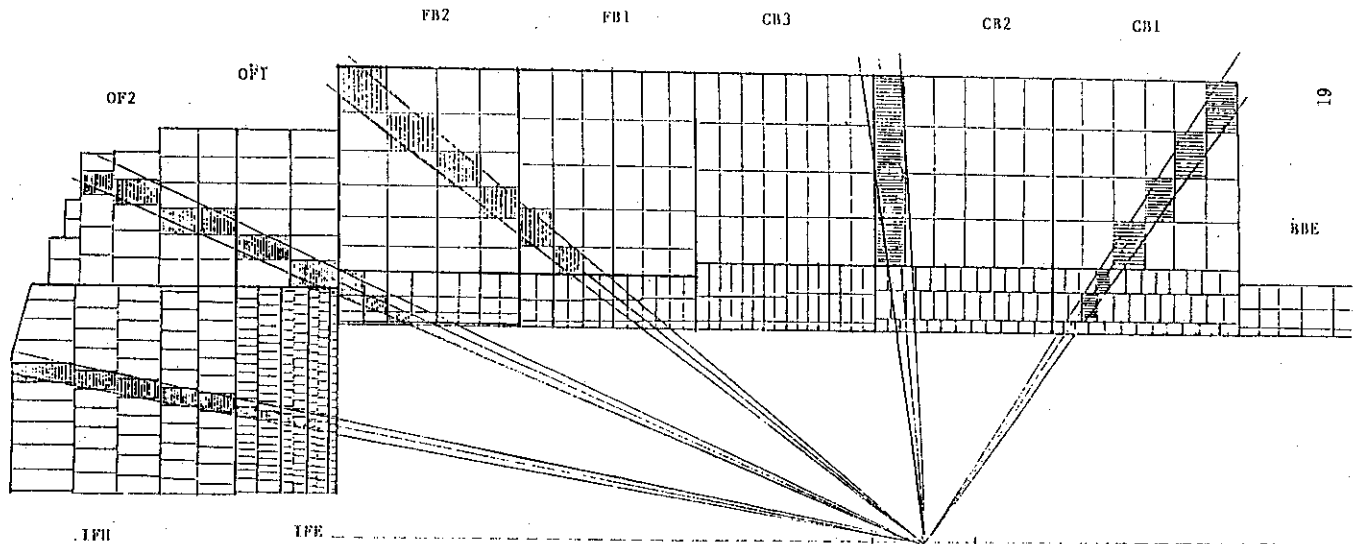


Figure 10: Transversal cross section of the calorimeter.

	Wheel	$\varphi$ -Segmentation	R x z Segmentation	# of channels	$\varphi$ -Segmentation	R x z Segmentation	# of channels
Backward Barrel $143^\circ \leq \theta \leq 152^\circ$	BBE	64	3 x 5	960	—	—	—
Central Barrel $45^\circ \leq \theta \leq 143^\circ$	CB1	64	3 x 12	2 304	64	4 x 6	1 536
	CB2	64	3 x 12	2 304	64	4 x 6	1 536
	CB3	128	3 x 16	6 144	64	4 x 8	2 048
Forward Barrel $20^\circ \leq \theta \leq 45^\circ$	FB1	128	3 x 12	4 608	64	5 x 6	1 920
	FB2	128	4 x 8	4 096	64	6 x 4	1 536
Forward $0 \leq \theta \leq 20^\circ$	IFE/OF1	128 64	16+16+15+14 10 x 4	7 808 2 560	64	6 x 2	768
	OF2	—	—	—	64	6+6+5+5	1 664
	IFI1	—	—	—	64	6+6+5+4+4	1 600
	TOTAL			30 784		6 x 5	960
							13 568

20

Table 4: Characteristics of the pad structure and of the number of electronic channels in the different parts of the calorimeter.



19

BBE

Figure 11: Segmentation of the calorimeter.

Wheel	Weight/ Wheel (t)	Total Area		Thickness Variation		# Samplings
		ROB (m <sup>2</sup> )	HV (m <sup>2</sup> )	LAr Gap ( $\mu$ m)	Plate ( $\mu$ m)	
IF2H	21.5	308	308	40	-	36
IF1E	8.6	277	262	30	60	64
OF2H	34	497	497	42	-	26
OF1H	20	300	300	38	-	17
FB1H	50	744	744	39	-	31
FB1E	6.6	27.6	27.5	30	55	46 / 70
CB1H	48	512	512	55	-	31
CB1E	8	832	792	40	45	42
BBE	4	16	15.9	25	45	46

Table 5: Characteristic parameters of the calorimeters.

The electromagnetic stack is a pile of G10-lead-G10 sandwiches which alternatively serve as high voltage electrode and read-out board segmented into pads [13]. The details of packing and supporting the stacks differ for the different regions of the calorimeter (see Sects 4.3, 4.4). The electromagnetic stacks were assembled separately from the hadronic stacks. They are coupled to their corresponding hadronic stack and locked mostly in the z-cracks. A different solution was chosen in the IF region where the half-rings are fixed to a single stainless steel tube bolted to the upper stack of the OF1H ring. The wheels were mounted in a horizontal position outside of the cryostat and inserted and supported by two rails. In Fig. 12, a wheel after assembly of the full ring is shown.

The free space between the inside part of the cryostat and the front of the electromagnetic calorimeter is filled with foam ("rohacell 51") which serves as an argon excluder.

In Tab. 5 some characteristic data of the full calorimeter (total sensitive area, weight of wheels, precision achieved) are collected.

### 4.3 Electromagnetic stacks

**Common features of the G10-lead-G10 sandwiches** Each electromagnetic stack consists of a pile of G10-lead-G10 sandwiches separated by spacers which define the liquid argon gaps. These sandwiches serve alternately as high voltage electrodes and read-out boards segmented into pads respectively. Because of the varying plate orientation and plate sizes, three different methods of piling up the sandwiches have been chosen.

The structure of an electromagnetic cell is shown in Fig. 13 (top). Copper clad read-out boards with the pad pattern on one side and the signal leads on the other side are glued with "prepreg" (glue film) onto both sides of the lead plates. The gluing of the FBE, CBE and BBE sandwiches was realized in the laboratories using a press in order to reduce the costs. The big IFE sandwiches have been produced in industry using an autoclave. The lead surfaces needed

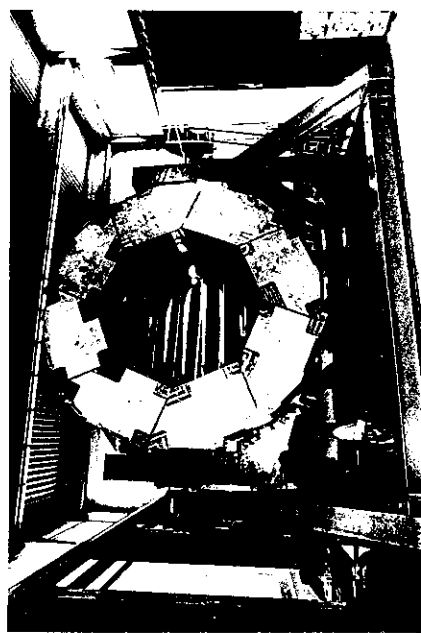
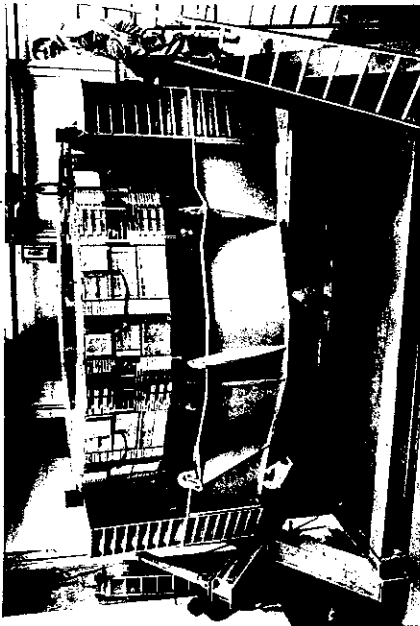


Figure 12: Pictures of the hadronic FB2 wheel during the rotation to the vertical orientation.

	IFE	FBE, BBE	CBE
Lead absorber	2.427	2.375	2.397
Read-out boards (incl. lead)	4.837	4.527	4.301
High voltage boards (incl. lead)	5.125	4.740	4.695
Liquid argon gap	2.370	2.338	2.336
Overall Cell	14.702	13.943	13.668

Table 6: Average thicknesses (mm) as measured at room temperature for the electromagnetic stacks.

a special treatment consisting of blasting with plastic spheres. The fresh surface was protected by a thin plastic film.

As shown in Fig. 13, a Kapton foil is glued with prepreg to the sandwiches of copper clad G10 and lead. A layer of high resistive coating consisting of a mixture of carbon and glue with a surface resistance of  $5 \text{ M}\Omega/\square$  is sieveprinted on a this foil afterwards. The high resistivity of the coating provides a high voltage protection while the Kapton foil serves as distributed decoupling capacity which allows to keep cross talk small.

The quality of the produced sandwiches was carefully controlled by measuring for each sandwich its weight and the surface resistance for high voltage sandwiches. In addition, the thicknesses of the copper cladding, of the kapton foil and of the lead plates were recorded, enabling characteristic parameters of the electromagnetic cells to be deduced. They are collected in Tab. 6 for the different types of wheels. The differences are due to the fact that different laboratories participating in the production placed their orders at different factories. Note that for a given wheel the parameters agree within the error limits. Hence the design goal for mechanical tolerances has been achieved.

A further important parameter is the gap thickness. It has been determined with mechanical devices and by capacity measurements respectively. The results are included in Tab. 6. A typical distribution for a stack is given in Fig. 14 measured with a mechanical device. In addition, the information on the variation of the thickness across the surface is available which can be used for correction when determining the calibration constants (Sect. 8).

**IFE stacks** The IFE stacks correspond to two half-rings with a vertical line of separation. In each half-ring the plates are bolted together by rods every 20 cm. Due to the large size of the sandwiches (2.5 m) the pressure by screwing the rods is only applied to the spacers not to the plates. The G10-lead-G10 sandwiches are just blocked between spacers without pressure due to the rods. After fixing the stacks in the stainless steel tube (Sect.4.2), the half rings are bolted together at the top and the bottom.

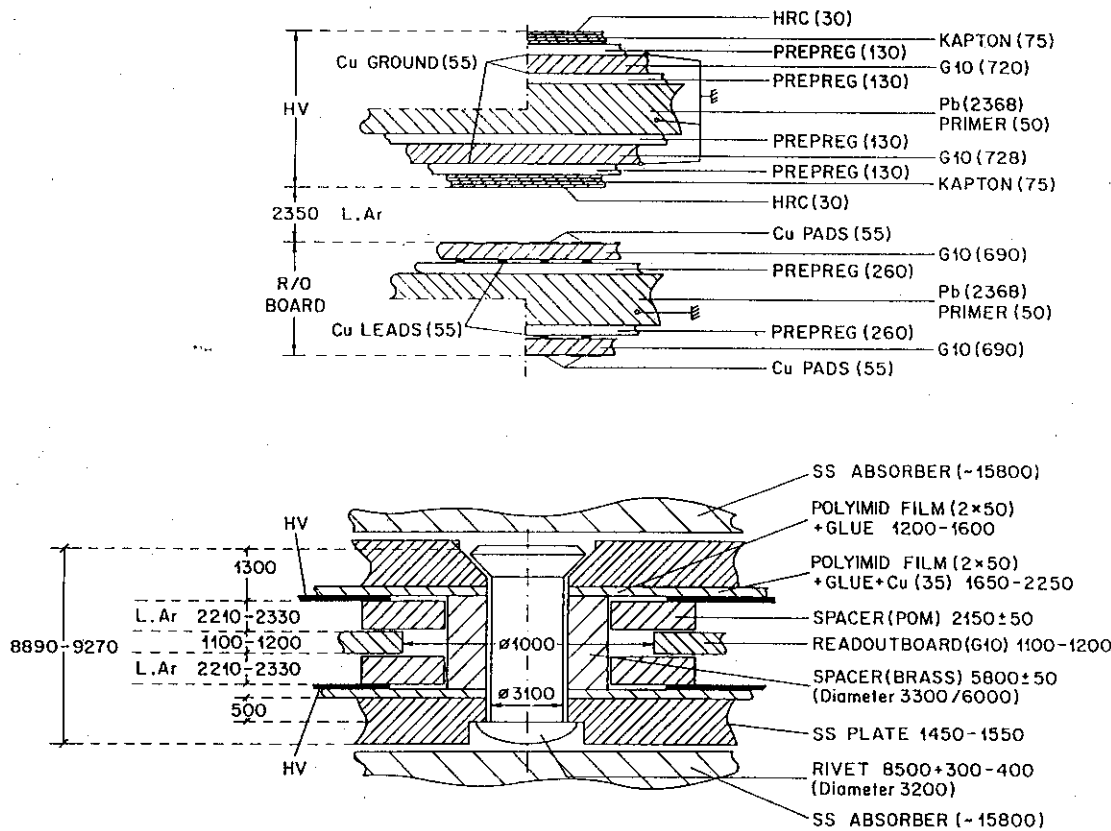


Figure 13: Schematic structure of an electromagnetic (top) and hadronic (bottom) read-out cell.

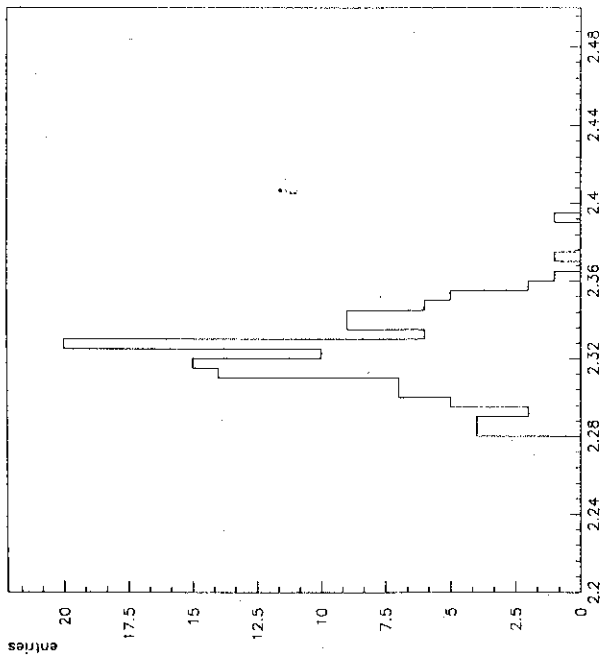


Figure 14: Measurement of the gap widths of an electromagnetic read-out cell.

**FBE, BBE stacks** The mechanical assembly of these stacks is similar. The sandwiches have the same trapezoidal shape for FB1E and FB2E. The design of the BBE sandwiches follows closely that of FB1E, but for a better coverage the octagon shape of a wheel is changed to a 24-polygon which approximates more closely the shape of the inner cryostat vessel. Nine steel rods, uniformly distributed on the surface of the plates and ended by springs fixed on one z-endplate, press the 120 sandwich plates together. The distance between high voltage and read-out plates is defined by spacers. The G10-lead-G10 sandwiches are not stiff enough to hold the forces on the rods. Therefore in the front-, the end- and the mid-plane the lead of two consecutive sandwiches is replaced by a 6 mm stainless steel plate in the first sandwich and a 0.8 mm G10 plate in the second one. It has been shown by Monte Carlo simulations and confirmed by test beam data that the homogeneity of the stack can thus be kept at the percent level [11]. The overall rigidity is guaranteed by 2 mm thin stainless steel plates in the  $\varphi$ -crack. Note that the BBE stacks consist of 80 sandwich plates only, therefore no mid-plane is necessary to stabilize the stack.

A similar hardware compensation of dead material as for the central stainless steel plate of the support structure has been applied in the region of the stainless steel rods by replacing a carefully chosen amount of lead near the rods by an aluminium ring. Again this hardware compensation of intrinsic inhomogeneities works at the percent level.

The FB2E sandwich has a specific feature which allows to use the pads of the front row of a stack for preshower measurements. To this end the lead core in this region of the sandwich is replaced by G10 material.

The FBE stacks are not self-supporting and are therefore coupled to the corresponding hadronic stacks. The BBE stacks are supported by the CB1 hadronic stack structures. During transport

Absorber structure	IFH	FBH, OFH	CBH
Stainless steel plates	15.79	15.86	15.75
Absorber gap	12.11	12.06	12.00
Independent read-out cell	9.72	9.46	9.22

Table 7: Average thicknesses (mm) as measured at room temperature for the hadronic stack a specially designed support structure had to be used to guarantee the required rigidity. E electromagnetic stack is attached at 2\*7 points to the hadronic stack.

**CBE stacks** The sandwiches have a rectangular shape, are parallel to the beam axis and have different sizes within a stack. In order to facilitate the production, all 24 CBE stacks have the same mechanics and dimensions. The gap between the sandwiches is defined by spaced every 100 mm on the read-out boards. The plates are pressed between a front-plate (inner radius) made of a composite light material and the first stainless steel plate of hadronic stack. The compression is maintained by a steel frame with plates perpendicular to the beam axis (z-crack) and with four rods located in the  $\varphi$ -cracks between two octants. With the exception of these rods the  $\varphi$ -crack is free of dense material and is reserved for the gang cables. Each CBE stack is coupled to the CBH stack by 2 x 3 locks in the z-crack, embedded in the stainless steel absorber plates of the hadronic stacks.

#### 4.4 Hadronic stacks

**Common features of the hadronic cells** The read-out cells are independent, self-supporting structures. Two stainless steel plates of 1.5 mm thickness define the active liquid argon gap using brass spacers and copper rivets. A sketch of the technical solution is shown in Fig. 13 (bottom). The distance between two spacers is of the order of 100 mm. A kapton foil is glued with prepreg layer to the inner side of the stainless steel plates, which is either coated by a high resistive layer (IF1, FBH, OFH) or with copper (CBH) on which the high voltage is applied. As for an electromagnetic stack, the kapton foil provides the decoupling capacitance necessary to keep negative cross talk low. While the high resistive coating provides automatically high voltage protection, for the copper solution neon spark gaps are added as active protection.

In the middle of the gap a G10 board with pads on both sides collects the charge deposited in the liquid argon gap. The pad sizes are typically four times larger in the hadronic than in the electromagnetic stacks. The hadronic boards have a typical size of 1 m<sup>2</sup>. ~100 m of 0.4 m wide insulation lines run on each side. 3200 boards of 110 different types have been produced at low cost, using special technology and equipment [13]. The distance between the G boards and the high voltage layers is defined by polyethylene spacers. The typical values of

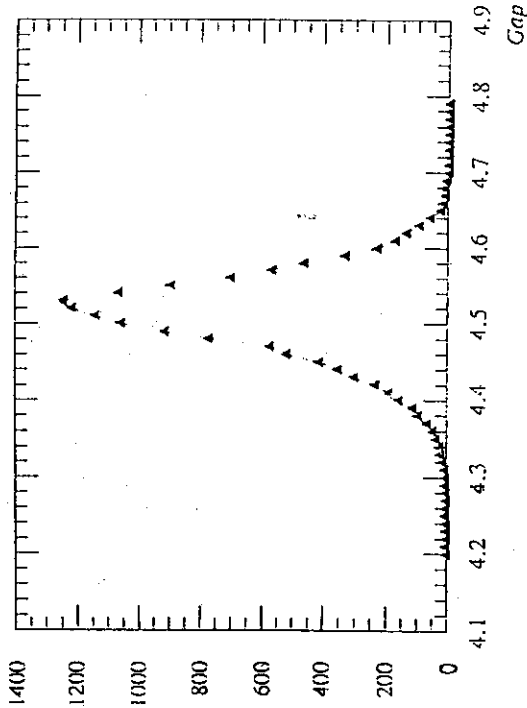


Figure 15: Measurement of the gap widths of a hadronic read-out cell.

mechanical parameters are collected in Tab. 3 and 7. After assembly the thickness of the two gaps per cell have been determined by a capacity measurement. A typical result is shown in Fig. 15. The achieved tolerance of  $\pm 1.5\%$  is in excellent agreement with the design goal.

**IFH stacks** The inner forward part of the hadronic calorimeter is divided into two half rings, with a horizontal line of separation. The absorber plates are welded together by seven bars pointing into the z-direction. The three back absorber plates have a smaller diameter adopted to the concave shape of the cryostat, they are individually screwed to the absorber plates in front. The complete IFH ring is supported by the OFH ring.

**FBH, OFH stacks** The vertical absorber plates of a ring have all the same size. The shape of the plates follows from Fig. 10. The plates are welded to five bars pointing along the beam axis, three of them at the outer and two of them at the inner radius. Almost no dead material is in the  $\varphi$ -cracks and the amount of dense material between an FBH and FBE stack is limited to two small bars. The locks which bolt each stack to the adjacent one are located at the periphery.

**CBH stacks** The absorber plates have a rectangular shape, are parallel to the z-axis and have all a different size within a stack. As for the corresponding electromagnetic stacks, all 24 CBH stacks have the same mechanics and the same dimensions. The welding of the absorber plates is done in the vertical plane (z-cracks) thus leaving the  $\varphi$ -cracks free of dense material and open for ganging cables. The last plate at the outer radius is thicker (30 mm) and reinforced by ribs. For the two stacks located below the horizontal mid-plane, skids are bolted to this plate, thus transferring the forces from the wheel to the rails in the cryostat. When assembled in a wheel, each stack is bolted to its neighbouring stack by  $2 \times 3$  locks arranged uniformly along

the radius in the z-crack. These locks are embedded in the plates thus avoiding an increase of the dead material in the z-crack.

#### 4.5 High voltage system

**Overall description** The high voltage to be applied to the liquid argon gaps is typically 1 kV/mm. In the present case this amounts to up to 2.5 kV. The high voltage is supplied via an external distribution system where voltage, leakage current and sparking are monitored. Shielded cables carry the high voltage to an entrance port at the cryostat where the shielding function is taken over by the cryostat wall. Single-lead cables are connected to flat cables which enter the cryostat via a special feed-through at the top of the expansion vessel (see Fig. 5). The number of high voltage connections has to be kept at a reasonable minimum to keep the cryogenic losses small. On the other hand, the volume of the stack which is supplied by one cable has to be kept small enough to minimize the effect of sparking in a single channel. Therefore we have chosen to supply areas comparable to one longitudinal sampling. The total voltage is fed via 1504 lines to the high voltage planes in each gap. Each line feeds a group of non-subsequent planes in a stack, interleaved with planes linked to a different line. There are no tower segment is completely dead in case of a problem on one high voltage line. On average twelve lines are used per electromagnetic or hadronic octant of each wheel. An example of the distribution of these channels to the various parts of an octant is shown in Fig. 16.

**High voltage distribution and control system** There are 56 independent high voltage sources, coming from two control crates, each with seven blocks of four high voltage generators. The 56 sources feed 56 distributors (located in 14 crates), each of them having 32 output channels. A 68K processor operated through an OS9 system controls the high voltage generators and the distributors via a VME bus interface and a serial transmission line. For each final high voltage channel the current is monitored with a full scale of 20  $\mu$ A and a sensitivity of 20 nA (respectively 200  $\mu$ A and 200 nA for some channels with high voltage problems). The processor is also linked to the general slow control system.

**Operation** The present operating voltage of the whole calorimeter is 1.5 KV which corresponds to an electric field of 650 V/mm. This is lower than the standard 1000 V/mm, but leads to a much more stable operation, minimizing the number of high voltage channels drawing high currents. The extrapolation of the collected charge to infinite high voltage is deduced from a fit to the high voltage curve.

## 5 Electronic System

### 5.1 Requirements

The design of the electronic system [14] had to take into account the situation of large energy being deposited at short time intervals (96 ns) into detectors with large capacitances and long charge collection times. In addition, the information has to be stored until the arrival of a trigger signal ( $\sim 2.9 \mu\text{s}$ ). Finally the liquid argon calorimeter has to be operated in a large magnetic field.

Particles crossing the drift gap ionize the liquid argon along their tracks. The generated charge carriers are separated and collected by a high voltage field across the gap. The charge signal is built up by the electrons drifting to the anode, whereas the influence of the positive ions is small and largely suppressed in the differentiated signal. The drift time is about 200 ns/mm and depends only slightly on the high voltage in the range considered here. An ionization electron with charge  $e_0$  deposited at a distance  $x$  from the cathode the measured charge is proportional to the drift path:  $Q(x) = e_0(d-x)/d$ , where  $d$  is the gap width. Integration over a uniform distribution across the gap yields half of the deposited charge measured charge.

In case of high counting rates, the length of the signal pulses has to be kept short and therefore small gap distances are necessary. In the H1 calorimeter a gap width of  $\sim 2.35$  mm is used corresponding to a drift time of 470 ns. The integration time has to be at least of this magnitude in order to accumulate all deposited charge.

For typical towers of the forward calorimeter sections the estimate of the electronic noise using the measured dependence of the electronic noise on the detector capacity  $C_D$  is:  $\sigma_n = 5500 e_0 + 5000 [e_0/nF] * C_D [nF]$ . Maximal signals are computed from GHEISHA simulations using electrons and pions of energies corresponding to the maximal two-body kinematic limit [15]. The ratio of the maximal signal to the noise is 19 400 in the electromagnetic part and 14 700 in the hadronic part. For 75 % of all channels a dynamic range of 12 bits is sufficient for the remaining 25 % a dynamic range of 14 bits is needed.

The smallest signal is typically that of a minimum ionizing particle. In the read-out configuration as defined for the hadronic calorimeters of H1, the charge  $Q$  collected from both gaps is given by  $Q [e_0] = dE/dx * 2d/2E$ , where  $E$  is the ionization potential (26.5 eV/ $e_0$ ) and  $dE/dx$  the energy loss of minimum ionizing particles (2.11 MeV/cm) in liquid argon. This yields  $Q = 18710 e_0$  for the charge deposited in a double gap of  $2 * 2.35$  mm. Correspondingly, the charge deposited in a single gap of the electromagnetic section is  $Q = 9355 e_0$ . The expected signals from minimum ionizing particles vary between 61 900  $e_0$  and 309 700  $e_0$ , depending on the longitudinal gauging. In order to detect this charge efficiently, a low noise amplifier is needed which has to have a variance of the noise peak of  $\sigma < 15000 e_0$  for an input capacitance about 1 nF as in the electromagnetic section of the forward calorimeter.

Due to the short bunch crossing distances at HERA, special care had to be taken to shorten the signal processing time. The probability that pile up occurs in a pad close to the proton beam during the processing of the signal is in the order of  $10^{-5}$ . The pile up problem in one channel does not seem too severe even accounting for the fact that the background is of high energy and spreads over several pads. However, the probability that there is 2 GeV of energy due to pile-up in conjunction with a good event somewhere in the detector is high (5 - 10%.

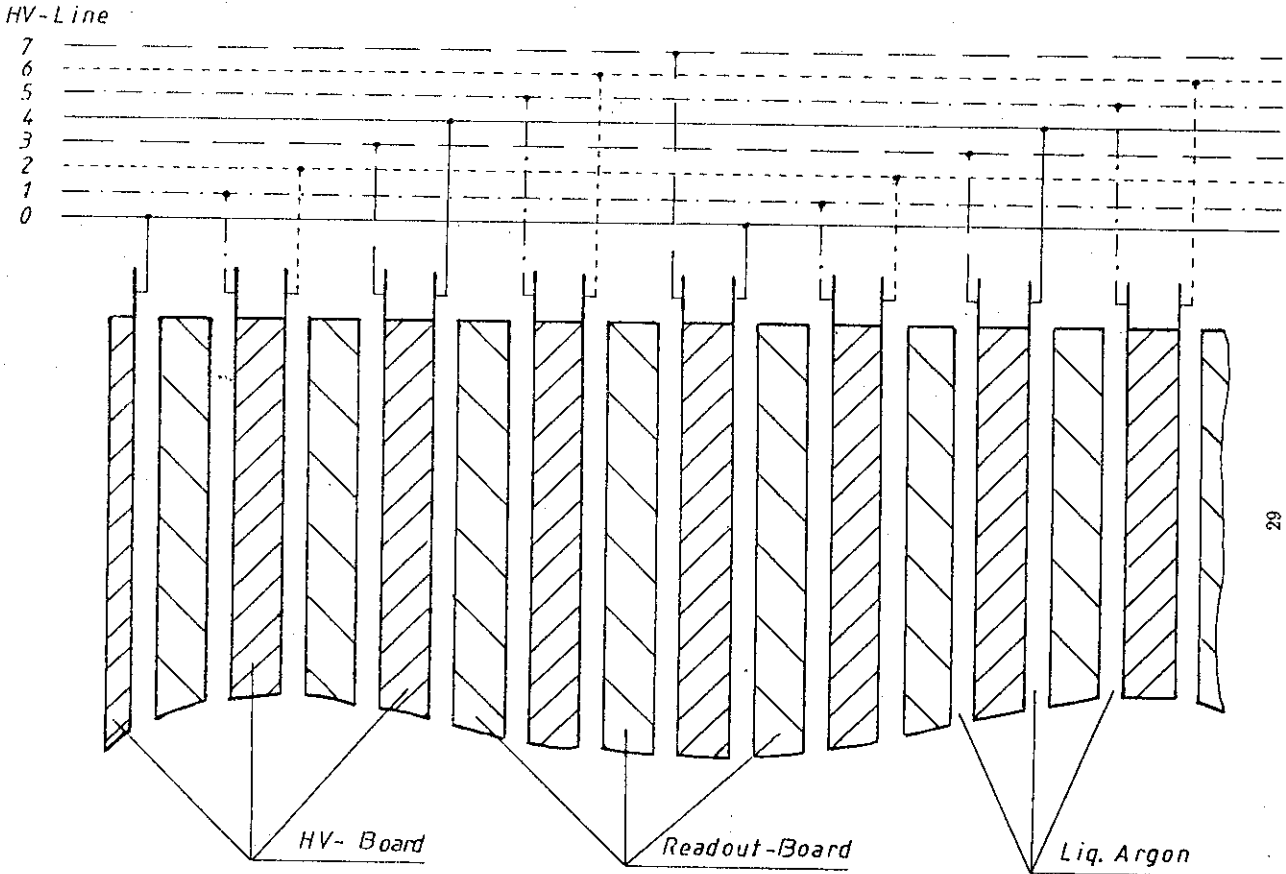


Figure 16: Distribution of the high voltage to the calorimeters.

## 5.2 Overall system

The individual read-out planes are ganged together on the side of each calorimeter module. The signals are transferred to the merging boards on the backside of the individual calorimeter modules where a regrouping into the final configuration is done. Calibration signals arriving from pulse generators located on the outside of the cryostat are applied here also.

Signal cables ( $\sim 10$  m long transmission lines of  $50 \Omega$  impedance) lead to the first stage electronics via the 24 feed-throughs of the cryostat [16].

Since the calorimeter is operated in high magnetic field, matching transformers cannot be used. The amplifiers have to be located as close as possible to the pad structure to reduce noise due to cable capacitance and to avoid slowing down signals due to the cable inductance. Thus the signal lines are fed out of the calorimeter into an analog signal processing chain consisting for each channel of a charge sensitive preamplifier (PA) and of a bipolar shaping amplifier. Upon trigger the peak signal is strobed into a sample and hold circuit.

The layout of the overall electronic chain is shown in Fig. 17. Sixteen channels are grouped on one analog card (ANCA), their analog signals are multiplexed 16/1. Eight analog cards are grouped into one mechanical and electrical unit called analog box (ANBX). Here they are linked to a service module, the translator card, which provides a second multiplexing (8/1). The signals are finally sent twice via two differentially driven twisted pair lines of  $\sim 25$  m to differential line receivers located in the analog receiving unit (ANRU). The double transmission with two different gains is used to extend the dynamic range to 14 bits. The amplification factors are either  $(1+2)$  or  $(1+4)$  depending on the ratio of the maximal signal expected from physics processes to the electronic noise in the different regions of the calorimeter [17].

For each analog card, a sum of the signals from each group of four adjacent channels as well as a sum of the signals from all channels is formed at the output of the preamplifiers. The summed signals are provided for the trigger.

For the CB and BBE calorimeters, the analog boxes are located near to the feedthroughs at the  $(-z)$ -side of the cryostat, while for the IF, OF and FB calorimeters they are located correspondingly at the  $(+z)$ -side.

The analog receiving unit performs the analog baseline subtraction. It serves four analog boxes, i.e. 512 electronic channels, and is connected to the ADC board. Each ADC board either serves 1024 channels coming via twisted pairs from two analog receiving units or 512 double gain channels coming from only one analog receiving unit. It consists of 8 ADC modules of 12-bit resolution which are read out and controlled by a DSP module located on a separate board. The whole set of DSP's is located in a VME crate and accessible to the DAQ system. The entire system is therefore designed for 14-bit dynamic range with 12-bit resolution. The DSP performs basic operations on the data like pedestal subtraction, zero-suppression and gain adjustment.

In Tab. 4 we summarize the number of channels for the analog chain. The total number of analog boxes is 353 and the total number of signal cables 3000.

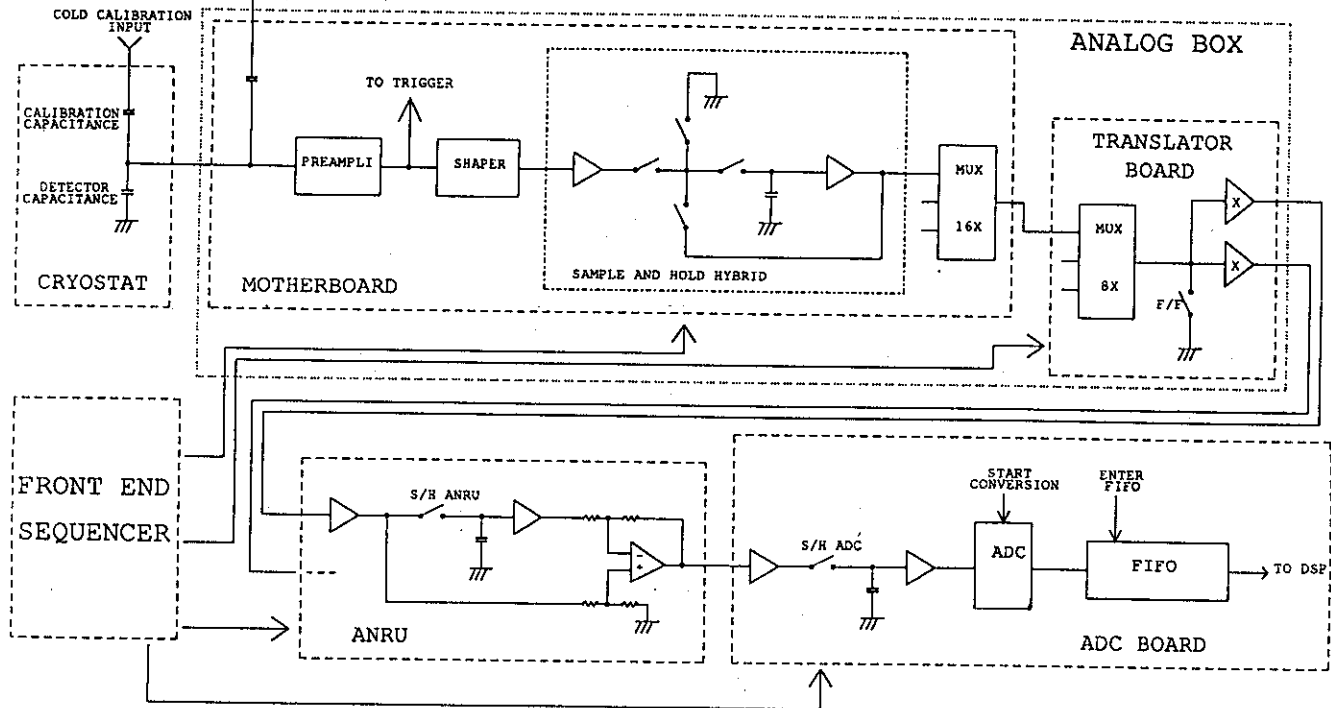


Figure 17: Schematic layout of the electronic chain.

### 5.3 Analog signal processing

**Preamplifier** The basic considerations for the application of low noise charge sensitive preamplifiers in liquid argon calorimeters have been outlined previously [18]. The input noise is proportional to  $(C_D + C_{par})$ , where  $C_D$  is the detector capacitance and  $C_{par}$  the parasitic capacitance (e.g. cables). Typical values are  $C_D \sim 5$  nF and  $C_{par} \sim 1$  nF. It is standard practice to match the calorimeter cell to the preamplifier via an optimally chosen transformer [19]. Due to the operation in a large magnetic field (1.2 T), other means to minimize the noise for large  $C_D$  have to be applied in the present case [20]: Very low noise JFETs are employed and longer integration times are used.

A protection of the preamplifiers against high voltage sparking is included in the motherboard. For each channel, it consists of a spark lamp, a series resistance  $R_S = 20 \Omega$ , and a protective transistor.

A single JFET (2SK372 Toshiba) is used at the input of the low noise charge sensitive preamplifier as the lowest noise device available. A large open loop gain of the amplifier of 95 dB is achieved for a maximal signal of  $280 \cdot 10^6 e_0$ , the feedback capacitor being  $C_F = 20$  pF. The maximal output voltage of the preamplifier amounts to 2.2 V.

The preamplifiers are built in hybrid technology, their dimensions being  $25.4 \times 16.9$  mm<sup>2</sup>.

**Shaping amplifier** The shaper [21] is a bandpass filter consisting of two passive high-pass sections and three active low-pass sections. Its purpose is to shape the incoming signal from the preamplifier into a bipolar signal with its peak amplitude at  $2.4 \mu s$ , and to supply this signal at an output voltage of 0 - 5 V to the sample and hold circuit.

The first high-pass stage has a time constant of  $0.975 \mu s$ . It works as a pole-zero compensation for the preamplifier time constant of  $40 \mu s$ . The second high-pass stage has a time constant of  $0.560 \mu s$ .

The active low-pass sections use the low-noise operational amplifiers of type LF351.M and LF353.M. The first and third stage together with the high-pass stages are the main shaping elements. They are realized as "Sallen-key" filters. They are designed with positive feedback, and have high input and low output impedances. The transfer function of each stage delivers two conjugate complex poles with characteristic time constants of  $\sim 0.5 \mu s$ .

The second low-pass stage is realized as a conventional filter with negative feedback. It is used to adjust to the detector capacitance. The time constant matches on average the peak times at the strobe.

The shaper is realized as a hybrid circuit of dimension  $38 \times 16.9$  mm<sup>2</sup>.

**Performance of the analog front-end** With this signal processing the noise depends on the detector capacitance as  $5.0 e_0 / pF$  with a constant term of  $3000 e_0$ . This value increases to  $5500 e_0$  if the entire chain is operated. These values refer to the actual input matching including the additional noise due to the protective resistance  $R_S$ . The linearity of the system of preamplifier and shaper was measured to be better than  $1/8000$ .

### 5.4 Transmission line and multiplexing

**Analog card** Besides preamplifiers, shapers and calibration lines, it houses the sample holds, the storage capacitors and the first stage multiplexer for 16 channels. It is linked to the translator card by a flat cable which transfers the command signals and is daisy-chained to eight analog cards, and by one line each for the multiplexer address and the output signal. The sample and hold configuration which has been selected is simple and inexpensive, performs rather well [22]. The non-linearity for signals that peak at  $\sim 2.7 \mu s$  is  $\sim 0.2\%$  over a 5 V range.

The principal disadvantage of such a simple configuration is the large, and potentially variable, charge injection pedestal produced by the CMOS switches. A double sampling configuration used which substantially reduces these pedestals and their variations [23]. After multiplexing the signal and its associated pedestal are stored in another, high quality sample and hold circuit. The storage capacitor is then discharged and a new, almost identical, charge injection pedestal is produced. The analog difference between the stored signal and the new pedestal represents the signal with nearly all of the pedestal removed.

An additional important advantage of this double sampling scheme is that it all but eliminates low frequency pick-up in the long cable between the multiplexer and the second sample and hold circuit, since the signals which are subtracted are only separated by  $3.5 \mu s$  in time. It should, in principle, reduce the effects of 50 Hz pick-up by about a factor of 1000. In practice a factor of 300 is observed, probably due to the limited common mode rejection of the second sample and hold circuit.

**Translator card** It is connected to its analog receiving unit by a single cable with ten twisted pairs. Six pairs are used for the command signals, two transmit the two gains, the last two used for test signal and ground. Special attention has been given to the following points:

- The conversion of the six ECL command signals in CMOS are made with inexpensive transconductance amplifiers (CA3080) except for the signal which defines the trigger order to improve the slew rate and the response time, it is converted by a special custom made amplifier, since for channels with low capacity, it is necessary to transmit the trigger signal as fast as possible.
- Since the analog signals may have amplitudes up to 8 V with stabilization and transient time of  $3.5 \mu s$ , it is necessary to use good performance line drivers (AD845).
- It has been found that some parts of the analog cards are temperature sensitive. That reason and also for test purposes, the translator generates two extra signals having sent the signals of the normal 128 channels: One is used to measure its ground and may be used to detect pedestal variations; the other one is used to monitor the temperature of the analog box as measured by a thermal gauge (AD590).

**Analog receiving unit** The analog receiving units are single slot VME like boards located in crates which house up to 20 analog receiving units each. A crate receives the synchronization signals from the front-end sequencer through a driver board for the analog receiving units. analog receiving unit has two functions:

- It is used to fan out the six ECL differential command signals (coming from the sequencer and distributed to a backplane bus by the driver board) to the analog boxes.

- It performs the analog baseline subtraction. For that purpose it has eight subunits. Each consists of a differential line receiver, a second high resolution sample/hold circuit (SHM20) for the subtraction and a subsequent differential line driver for the connection to the ADC board.

**Front-end sequencer** It is responsible for the sequencing of the entire analog chain. It mainly produces the phases for the switches of the sample/hold hybrids and the channel count for the multiplexers [22]. It also sends synchronization signals to the ADC Board. It is built as a single VME unit, all parameters are thus VME accessible. If the channel count is fixed, it is possible to view the shaper response of any analog channel at the level of the analog receiving unit with an oscilloscope.

## 5.5 ADC and read-out system

**Overview** The outputs of the analog receiving units are connected to an ADC board coupled to a Digital Signal Processor board; each pair processes the data of up to 1024 channels.

**ADC** The ADC board consists of eight identical modules each digitizing the data of 128 multiplexed channels. Thus each ADC Board converts either single gain data of 1024 channels or double gain data of 512 channels (see above). One module consists of a pair of LF347 line receivers, an SHM20C Sample and Hold, an AD7572 ADC and a buffer where the data are latched in by the DSP sequencer at each conversion cycle. This 12-bit ADC has a conversion time of 5  $\mu$ s. The ADC Board has a 4-layer printed circuit with all components except the SHM20C in surface mount technology. It is located in a special crate providing the power supplies, each board occupying a single slot and interfaced to its DSP board by a 1.5 m flat cable connecting both P2/J2 connectors on the backplane.

**DSP read-out** A specially designed DSP board based on the Motorola DSP 56001 [24] is used to process the converted data. Details on the tasks performed by these DSP's are given in the section on data acquisition. Synchronization for the ADC conversion is provided by a programmable sequencer located on the corresponding DSP board and triggered by the main front-end sequencer for each of the 128 conversion cycles per event. In each DSP crate (maximum of 17 ADC/DSP sets) a service module interfaces the signals between the trigger fan-out, the front-end sequencer and the DSP's. In addition, it has a local clock and trigger functions for stand alone tests.

## 5.6 Calibration system for the electronic chain

The layout of the calibration system for the electronic chain is described in [25]. In order to maintain the excellent calorimeter resolution, it is necessary to correct for different electronic gains of individual channels. This is determined by a precise measurement of the ADC response to a known charge injected at the calorimeter pads. Moreover, the calibration procedure allows

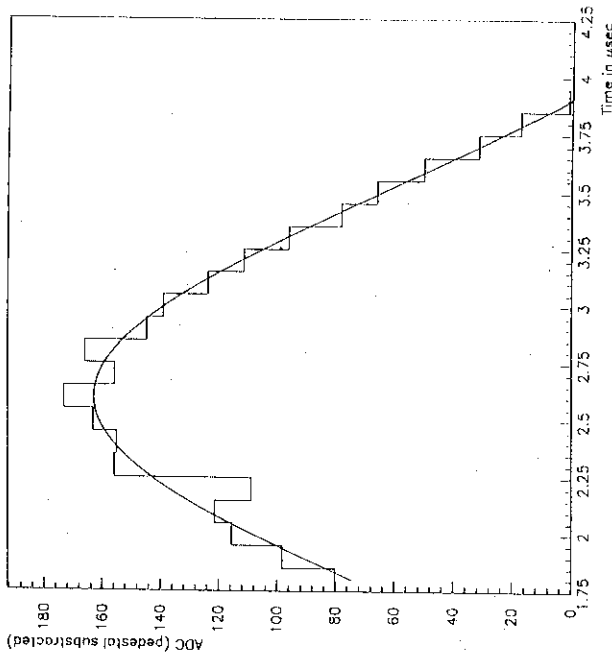


Figure 18: Time adjustment of the calibration with respect to the particles.

for crosstalk determination as well as for hardware monitoring during long periods of data taking.

**Calibration set-up.** The calibration hardware consists of a set of pulse generators steered by four command modules. Each generator may simultaneously pulse at most 64 channels command module activates selected groups of generators and sets the level of a voltage pulse a 16-bit DAC. The output voltage varies between -1 and 0 V. It charges 47 pF calibration capacitors (1% precision), this value allowing to cover the total dynamic range of the calorimeter. Two calibration systems are used: In the 'warm' system the signal is injected into capacitors near the preamplifier level, and in the 'cold' system it is injected into capacitors located in the liquid argon near the calorimeter pads. These capacitors are placed on the merging boards on the of each stack where the transition between ganging cables and signal cables is done. In total 992 (768) generators are needed for the cold (warm) calibration of all channels of the liquid argon calorimeter. The distribution of the calibration signals follows a flexible scheme where one generator pulses one channel out of a group of 12 or 16 depending on the pad configuration of a given stack. Thus detailed cross-talk studies may be performed.

The calibration signals should reproduce the calorimeter signals as closely as possible. This is achieved by a calibration signal which has an exponential form with a time constant which corresponds to the charge collection time in the liquid argon divided by a factor of three. Since the calibration signals are injected close to the calorimeter pads, they depend on the time and on the pad capacity like the signals from real data. Moreover, a manual adjustment of each generator card ensures that all the signals coming from the generators arrive at the same time at the injection capacity.

**Calibration procedure.** At first, the calibration chain is timed with respect to the particles by adjusting the shaper responses of both sources to a common function. This is shown in Fig. 18 where the histogram corresponds to the signal seen at the CERN test beam in one electromagnetic channel and the curve is fitted from the calibration. The calibration system is used for two functions:

- Long term: A high precision determination of the calibration curves (ADC response vs. injected charge) is done each time changes in the hardware occur. Here the calibration of the electronic chain is a two-fold procedure: In a first step, mean value and width of the response distribution are calculated for each channel at each calibration point. Then a fit to a third order polynomial is performed according to:

$$Q = \sum_{n=1}^3 p_n * (ADC_{count} - pedestal)^n$$

The absolute precision of the calibration output is of the order of 0.1 - 0.2% at each generator output.

- Short term: Day-to-day fast monitoring of the hardware and of the reliability of the electronic calibration.

The time stability of the calibration parameters is demonstrated in Figs. 19 a, b and c. For the very few channels ( $\ll 1\%$ ) which do not respond to the cold calibration a special algorithm based on the warm calibration is used, providing a high security for a possible later loss of cold calibration lines [26].

**Calibration monitoring.** The calibration system has its own monitoring system built into the DAC modules. For each generator, this module is able to measure the level of the output voltage and of the ground with an ADC and a set of multiplexers. Measurements are made either absolutely or differentially with the DAC value, in the latter case with an accuracy of 250  $\mu$ V. Module to module comparison is also possible. This is particularly important for the comparison with the module which is the basis of the energy calibration with beam. The results show that the dispersion in the generator gains is  $2 * 10^{-3}$ , the stability of the generator being 10 times better as seen in Fig. 19 d.

## 5.7 Performance of the electronic system

The performance [27] of the electronic system has been measured using the data acquisition system and operating the calibration in various configurations. Results are shown in Tab. 8, they refer to the whole liquid argon calorimeter.

- The first five items in Tab. 8 show the timing quality of the system. The most critical items are the timing of the cold generators which has to be better than  $\sim 5$  ns in order to accurately adjust the calorimeter trigger, and the accuracy to which the calibration timing is known with respect to the beam particles [28] [29].

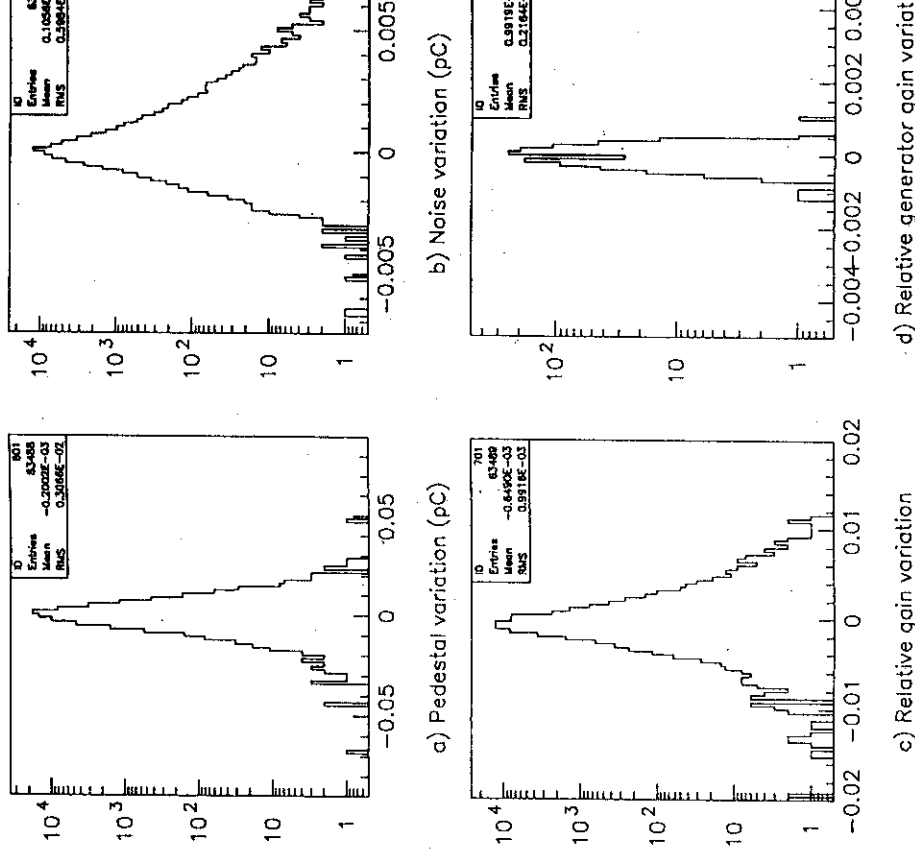


Figure 19: Time stability of the calibration chain over a period of one month.

## 6 Calorimeter Trigger System

### 6.1 System overview

The requirements imposed on the first level liquid argon calorimeter trigger system by physical considerations are outlined in a separate report [30]. We address here only the technical realization which is described in detail in ref. [31].

The calorimeter trigger is divided into an analog and a digital part. The task of the analog electronics is to reorder and combine the signals from 45 000 read-out channels in an analog into 256 projective towers, called 'Big Towers' (BT), which are divided into electromagnetic and hadronic sections. These 2 \* 256 big towers are digitized with fast (10 MHz) FADC's and fed digital summing electronics yielding various energy sums (e.g. total energy, transverse energy etc.). The sums are discriminated employing programmable threshold functions, providing trigger bits for the central trigger processor.

In the analog part, the big tower granularity is achieved in two steps: The primary input of the trigger system is a 'Trigger Cell' (TC), receiving its differential signals from the preamplifier boxes via twisted pair cables. Each trigger cell is an analog sum of 16 pad signals in electromagnetic or 4 in the hadronic part. Up to 4 electromagnetic and 6 hadronic trigger cells are summed and shaped, they form the raw inputs to build a 'Trigger Tower' (TT). Trigger tower outputs are still separated into electromagnetic and hadronic sections. In order to suppress noise at this stage of analog summing, the trigger tower signals are gated by analog switches only if they exceed a minimum amplitude, set by external controls.

Finally, the big tower is a sum of up to 4 trigger towers where the finest granularity is realized for small polar angles with respect to the proton beam. Synchronous to the bunch crossing frequency of 10 MHz, the big tower analog signals are digitized and stored for later access by the data acquisition system. Further signal processing is purely digital. Both the electromagnetic and hadronic sections are added to total big tower energy sums after relative weighting by lookup tables. These big tower energy sums are used to calculate and discriminate the following quantities:

- Topological energies in various parts of the calorimeter, such as central barrel, forward barrel, inner forward barrel, BEMC and Plug. For each of these regions the energy sums are calculated for each azimuthal quadrant are also available.
- Energy in the barrel part (CB and FB)
- Energy in the Forward Calorimeter (IF + Plug)
- Energy in the Backward Calorimeter (Barrel + BEMC)
- Transverse energy
- Missing transverse energy
- Weighted energy in the calorimeter

The geometrical weighting of the big towers is done via lookup tables which are programmed

Quantity	Unit	Average	Rms	1 % limit
Cold generator timing	$\mu s$		0.012	0.030
Warm generator timing	$\mu s$		0.016	0.030
ANBX timing	$\mu s$		0.031	0.080
Shaper timing	$\mu s$		0.026	0.048
CERN timing	$\mu s$		0.005	
$R^{cold}$	$\mu s/nF$	0.041	0.004	
$R^{warm}$	$\mu s/nF$	0.021	0.002	
$B_{noise}$	$e_0/nF$	3498	3.2	
$A_{noise}$	$e_0$	11325	17.3	
Crosstalk	%	0.8	1.1	4.
ADC-to-charge fit	%	0.06	0.06	0.25
Non-linearity	%	0.42	0.4	1.5
Gain stability	%		0.1	0.25
Pedestal stability	fC		0.4	1.2

Table 8: Summary of the performance of the electronic chain.

- The next four items refer to quantities which depend upon the detector capacity  $C$ :

$$t_{max}^{cold} \approx R^{cold} C$$

$$t_{max}^{warm} \approx R^{warm} C$$

$$\sigma_{pedestal} = A_{noise} + B_{noise} C$$

where  $t_{max}^{cold,warm}$  are the times when the signal at the shaper output is maximum for the cold (warm) calibration respectively, and  $\sigma_{pedestal}$  is the measured noise.

- The last four items are figures of merit for the ADC to charge conversion. "ADC-to-charge fit" denotes the accuracy of the 3<sup>rd</sup> order polynomial fit.

In addition to the energy sums, the digital part of the calorimeter trigger also counts big towers with given energy depositions in the electromagnetic and hadronic sections. In this way electron triggers can be derived by e.g. requiring more than a minimum energy in the electromagnetic section and less than a maximum energy in the hadronic section of a given big tower. The total number of big towers fulfilling these criteria is counted at each bunch crossing.

For each of these signals, various discriminator levels are foreseen which can be remotely controlled, thus determining the desired trigger energies or big tower numbers.

Besides the fast determination of energy sums and big tower numbers, the trigger has the task to determine the exact bunch crossing of the energy deposition ( $t_0$ ). This is done in the analog part by means of a pulse delay and crossing technique at the trigger tower level: The crossing point of the original and of the delayed trigger tower signal is determined and compared to an amplitude window to exclude noise and saturation effects. The gated  $t_0$  signals are then synchronized with the bunch crossing signal and counted. A number discriminator provides a  $t_0$  signal to the central trigger logic.

The entire processing of the trigger signal is pipelined. Between the bunch crossing numbers 12 and 13 after the event, the  $t_0$  signal is generated and the FADC's start the digitization. The next clock pulses shift the data through the digital address trees which need about 8 bunch crossings for the complete summing. At bunch crossing 21.5 the output signals of the discriminators are fed into the central trigger logic.

## 6.2 The analog part of the calorimeter trigger

The schematic arrangement of the analog part of the calorimeter trigger is shown in Fig. 20.

**Summing and shaping module (SSM)** The module contains four identical channels, each collecting the input data for one trigger tower. The line receivers accept differential signals from the various trigger cells via twisted pair cables. Each single receiver can be enabled or disabled by remote control of analog switches. Up to 4 electromagnetic and 6 hadronic trigger cells can be summed separately. The summing amplifiers feed their outputs into identical shapers with a time constant of 200 ns. In addition, the total energy sum (electromagnetic and hadronic) of the trigger tower is formed. This signal is shaped with a time constant of 100 ns and is used to determine the  $t_0$  time (see below). The two types of shaping amplifiers represent bandpass filters which have the same structure. The shaping amplifier consists of two active low-pass sections and two passive high-pass filters, realized by two different time constants.

The shape and the timing of the output voltage for a given input current depend not only on the shaper function but also strongly on the detector capacitance. Since this capacitance is very different in different parts of the detector, the peaks of the corresponding output signals will appear at different times. Since high accuracy of the bunch crossing time is required, a perfect pole-zero compensation for the input time constant is necessary. This is realized in the transfer function of the summing amplifier. To this end the RC-time constants in all input ports of this amplifier can be adjusted individually so that the corresponding detector time constants are cancelled.

Pad capacitances range from 1 to 15 nF over the whole detector. However, the signals from the first summing stage within a given trigger cell come from gaps having similar capacities within

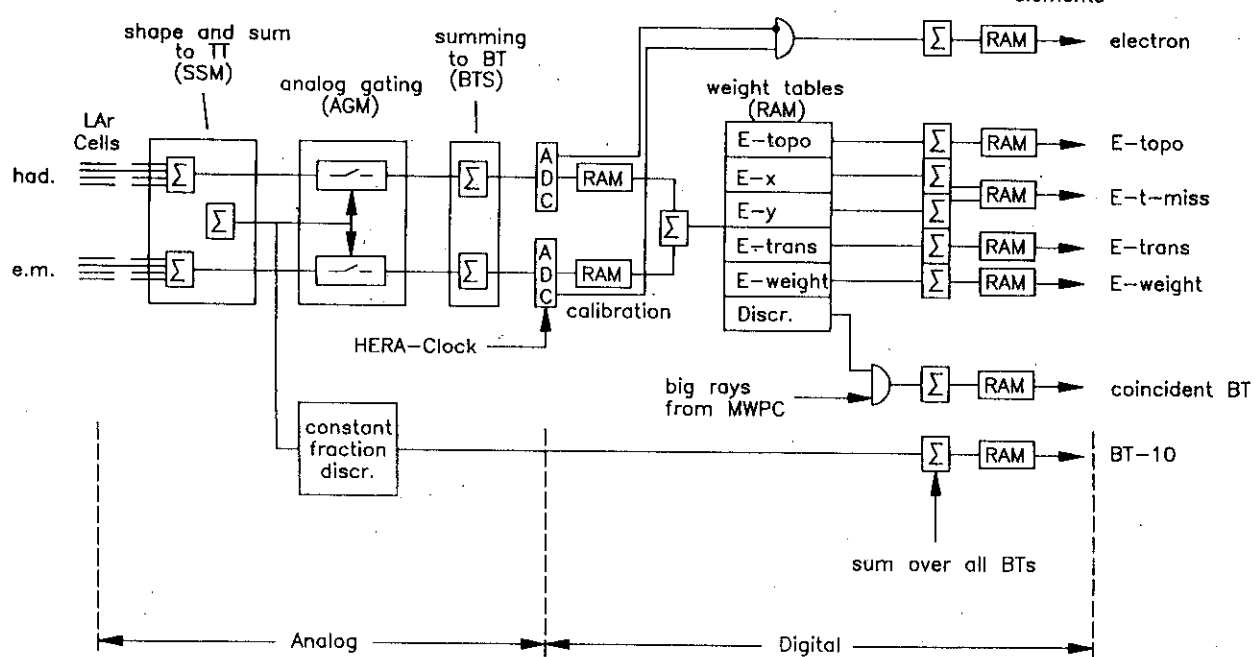


Figure 20: Schematic layout of the chain of the calorimeter trigger.

$\pm 5\%$ . Otherwise, the  $t_0$  signal could be shifted to a wrong time slice.

**Analog gating module (AGM)** In order to keep the summed noise as small as possible, only those channels containing a certain minimal energy are added together. The total trigger tower energy signal delivered by the summing and shaping module is compared to a computer controlled threshold presently set to  $5\sigma$  ( $\sigma = 250$  MeV). If the signal exceeds it, two fast analog gates are opened to guide the electromagnetic and the hadronic energies of a trigger tower to the summing stage building the big towers. The analog switches are realized with very fast MOSFET's. The injected charge is compensated by a reverse signal. Eight trigger towers are processed in this way on an analog gating module.

**Big tower summing module (BTS)** In this module the signals of trigger towers are summed to build big towers. The number of summed trigger towers (between one and four) depends on the position of the trigger towers within the calorimeter. Each big tower summing unit provides the signals from eight big towers to the digital part of the trigger separately for electromagnetic and hadronic sections. A big tower summing module contains 32 summing amplifiers and 32 signal splitter/drivers. The second output is an option for another set of FADC's which may be used for a fast higher level trigger processor.

**$t_0$  determination** The  $t_0$ -modules determine the exact timing of the event, i.e. the bunch cross number of the  $ep$  interaction. The energy signal from the trigger tower is delayed and compared with the undelayed signal. The crossing time of the two pulses defines the relative event timing. It is synchronized to the next HERA clock cycle. Sixteen trigger tower signals are processed in one  $t_0$ -module.

There are three different timing classes for the signals generated in the summing and shaping modules and in the  $t_0$ -modules due to the large differences in detector capacities. Since the signals have to be counted for every bunch crossing, these differences are compensated in the TUF-module. At the output of this module all  $t_0$ -signals coming from one event appear at a single bunch crossing period and are ready to be counted.

Since the sum of all  $t_0$  signals has to be available for every bunch crossing, the summing is done in the pipelined  $t_0$  summing module. The first summing stage is done in lookup tables, the further in binary adders. In order to be as fast as possible, the overflows are treated separately. The final pipeline stages and the comparators which send the trigger signal to the central trigger logic are assembled in the module SUMKA. This module is connected to the computer via VME and allows the loading of digital thresholds for the lower and upper limits on the number of  $t_0$  signals generating the event timing.

**Control module (CNTRL)** The control module is the main connection of the analog part of the trigger to the computer. All analog thresholds and the switches for the input to a summing and shaping module can be set via this module. The enabling/disabling feature of input channels requires digital control logic for the computer connection. A 40 Bit wide write/read register controls the analog switches in the receiver circuits.

**Mechanics** The analog part of the trigger is arranged in five racks containing five V crates each. The crates in turn house between four and eight summing and shaping modules (172 units in total), one or two big tower summing units (32 in total) and one or  $t_0$ -modules (44 in total). For the  $t_0$  determination, 16 TUF modules, four  $t_0$  summing units and one SUMKA are needed. In addition, various modules for clock distribution, VME-interface and thresholds are necessary.

### 6.3 The digital part of the calorimeter trigger

The schematic arrangement of the digital part of the calorimeter trigger is shown in Fig. 2

**FADC front board (FB)** The digital part of the first level trigger processor starts with the FADC's as digital data sources. They convert, synchronous to the bunch crossing signal every 96 ns the various big tower signals into eight-bit wide words which are stored into RAM for later read-out. The RAM's are 256 bunch crossings deep so that a history of 2.5  $\mu$ s be stored. The relative weighting of electromagnetic and hadronic big tower energies is done using lookup tables. The two components are added after weighting to get the total big tower energy. On the big tower level a number of functions are carried out in addition: Each of big tower components is digitally discriminated in order to determine big towers with an energy deposition characteristic for electrons, i.e. large energy deposition in the electromagnetic small energy deposition in the hadronic part. Furthermore, the individual big tower component exceeding a presettable energy threshold are flagged ('trigger bits') for later processing in special digital signal processors for the trigger data (DSPT's, see Sect. 7).

There are four big tower processing channels on each front board which need eight FADC and the necessary control logic. RAM's and lookup tables are accessible via VME bus. Processing of the trigger data in this module takes three bunch crossings in the pipeline.

**Digital mid board (MB)** In order to compute the different trigger quantities mentioned above, the total big tower energies have to be weighted with various functions. Again this is done using lookup tables. For each trigger quantity the big tower energies are transformed to the corresponding outputs to be summed up in consecutive digital adder trees. The final partial sum is evaluated in the mid board to reduce the amount of connections to the subsequent summing units. Each mid board is associated to a front board, building the various partial energy sums from the 4 big towers in the front board. The results of this first summing stage are stored in local RAM's with a frequency corresponding to the HERA clock, 256 bunch crossings deep. For the determination of the missing transverse energy the components  $E_x$  and  $E_y$  separately calculated including the sign, thus reducing the accuracy to seven bits. In addition the discriminator outputs from the electromagnetic and hadronic parts of the big towers are evaluated to set the corresponding bit for an electron, to set the bits for big towers above given threshold ('big-tower- $t_0$ '), or to set the bits for big towers pointed at by tracks from central chambers ('big-ray- $t_0$ ').

**Digital adder tree** Three further levels are needed to sum up the various quantities. The first stage is done on the adder boards (AB), located in the FADC crate. The resulting partial sums are fed into the topological boards (TB), where the weighted quadrant and total sum

in the various topological areas are built. Finally, the summing board (SB) calculates the total quantities over the entire calorimeter. As to the determination of the missing transverse energy, the vector sums of the two components  $E_x$  and  $E_y$  are computed individually. Counting of electrons, big-tower- $t_0$ 's and big-ray- $t_0$ 's are done in the bit boards (BB), in analogy to the summing board, after an initial summing stage at the FADC crate level (EDSPB for counting of electrons and BRBTB for that of big-tower- $t_0$ 's and big-ray- $t_0$ 's counting). The digital discriminators for the trigger quantities are located on the topological board, summing board and bit board. They are realized as lookup tables, again 256 bunch crossings deep and eight-bits wide.

There are various possibilities of adding 256 eight-bit words. In this system, five times 256 weighted big tower signals have to be summed. Serial accumulation would disturb the pipelined structure of the system, while parallel summing would need a large amount of logic. A total of eight planes of adders are necessary to get the final result. With standard integrated circuits this would take about 1000 four-bit adders for one adding tree. Together with the necessary storing elements for the partial results and line driving circuits, the system would not be practicable. In order to reduce the component number and the crate and rack space, a gate array solution was realized. It contains a four-word eight-bit adder with input registers and overflow handling. It adds the four words in 70 ns in two adding planes.

**Mechanics and interface** The digital part of the trigger is arranged according to a geometrical ordering scheme in two racks with five VME crates each - four FADC crates and one adder crate. Each FADC crate houses eight front boards, eight mid boards, one adder board and a controller board (CB) for VME communication. Because of the fine granularity in the forward direction, one rack services only the inner forward and PLUG regions, while the other houses the forward barrel, central barrel and BEMC regions. In total the adder crates contain five topological boards, eight summing boards, and four bit boards. The system is interfaced with VME and with the DSPT's (described in Sect. 7). When the first level trigger has stopped the pipeline, these processors read-out the digital information stored in the modules described above for a preselected number of time slices around the event  $t_0$ , suitably zero suppressing all big towers below a minimum energy. Each of the ten digital crates is associated with one DSPT so that the entire system is read-out with a high degree of parallelism.

## 6.4 Performance of the trigger

The overall decision time of the calorimeter trigger chain is 21.5 bunch crossings or 2.1  $\mu$ s. The precision of the  $t_0$  determination is 10 ns for a single trigger tower over the full dynamic range and 20 ns for the entire system. The intrinsic noise within a trigger tower (electromagnetic or hadronic part) ranges from about 250 to 400 MeV ( $1 \sigma$  limit), depending on the channel capacity. Trigger thresholds of 2 GeV have been achieved for electrons, and 4 GeV for the total energy quantities such as transverse and missing transverse energy.

## 7 Data Acquisition and Monitoring

The overall layout of the data acquisition and monitoring system for the H1 calorimetry, including warm calorimeters, is shown in Fig. 21.

The basic data used for the liquid argon calorimetry measurement consist of about 65 twelve-bit ADC values taking into account double gain channels. In addition, extra data are needed to monitor the pileup effects: the expected HERA proton beam gas and beam window rates lead to an average of 2 pileup events hitting the calorimeter during the 10  $\mu$ s time sensitivity of the liquid argon analog electronics. This is controlled by reading the history of the trigger signals from the 512 big towers which are available in FADC memories (256 memories (256 bunch crossings deep)). The primary data flow from the front-end electronics thus amounts globally to 1/4 Mbyte and is equally shared between the calorimetry and trigger data.

These data must be read out following the constraints imposed by the expected high rate background triggers: Read-out is initiated by the L1/L2 hardware trigger at a rate of a few hundred Hz. It should free the front-end electronics for a new event in less than 800  $\mu$ s. During this time, it should be interruptible by an L3-reject trigger decision and resetttable in a few  $\mu$ s. The L3-kept events should be logged to the H1 central data acquisition at a rate of 50 events with less than 10% dead time. Meeting these constraints requires a large amount of front-end processing power performing a strong data reduction, with the additional goal of providing data in a form directly usable by the off-line reconstruction.

The first level of front-end processing is done on a channel-by-channel basis by a set of Digital Signal Processors based on the Motorola DSP56001 chip [24], providing altogether 700 MHz of parallel processing power. Two different boards were designed to match the interfaces of the calorimeter ADC's and the trigger FADC's respectively. On the calorimeter side, 69 DSPT's (DSFC) perform:

- a noise suppression in absolute value (keeping negative values),
- an electronic calibration correction using the coefficients from a third order polynomial fit,
- gain selection for double gain channels,
- a geometrical numbering of channels.

On the trigger side, 11 DSP's (DSPT):

- check the timing of the big tower data,
- estimate the pileup signal per big tower (energy and deposition time),
- read-out the results of the digital summing tree.

The set of DSP's outputs a data flow of 10 to 20 Kbyte per event which corresponds to a reduction factor of 20 compared to the input flow.

The second level of front-end processing is done on an event basis by two event builders processing the calorimeter and trigger data separately. For this purpose, a special board based on

AM29000 RISC processor [32] was developed running the VRTX real time kernel [33]. Starting on the L3-Keep trigger signal, the event builders act as block movers gathering the DSP data, formatting them and logging them to the central data acquisition through a multi-event buffer. In addition, the processing power of the AM29000 allows to perform simple monitoring tasks like channel map histograms.

The liquid argon data acquisition system involves more than 200 VME boards spread out over 40 VME crates (Fig. 21). All crates are interconnected by the Vertical Bus (interfaced with the CES VIC8250) providing FASTBUS like features. The whole system is controlled by a central OS9 station connected to a VAX cluster by a dedicated VMEbus-Qbus link. The main purpose of the OS9 station is to run a VME server defining the configuration of the hardware (DSP's, event builders, calibration, trigger) according to user requests. It also provides basic checking procedures in a convenient multi-user environment. The VAX cluster can make direct requests to the OS9 VME-server through the Qbus link. This is used for sophisticated calibration procedures involving both calorimeter and trigger branches in connection to the ORACLE data base. The VAX cluster also runs online monitoring programs processing events requested from the event builders through OS9 during data taking.

More details on the H1 calorimeter data acquisition system can be found in [34].

## 8 Energy Measurement

### 8.1 Procedure for energy calibration

The charge  $Q_0$  deposited in the calorimeter follows from the recorded signal after having taken into account pedestal fluctuations, cross talk and noise cuts. The measured charge  $Q$  is converted into an energy using beam data collected at the CERN SPS [11, 35]. Since the experimental conditions at the test beam are not identical to those at the H1 detector, an ideal calibration constant  $c_{id}^{em} = E_{dep} / Q_{id}$  has to be defined, where  $E_{dep}$  is the energy deposited in an ideal stack and  $Q_{id}$  is the corresponding detected charge. An ideal stack is defined by the following conditions:

- The gap and absorber thicknesses are homogeneous and correspond to the nominal value.
- No dead material is positioned in front of the stack.
- The liquid argon is not polluted.
- The calibration capacities of all channels have the nominal value.
- There is no electronic noise.

The corrections due to e.g. dead material in front of the calorimeter, or the noise cut follow from Monte Carlo simulations [11, 37].

Electromagnetic scale for electromagnetic calorimeters The charge  $Q$  measured with a calibration stack at the CERN SPS beam is corrected for the following effects:

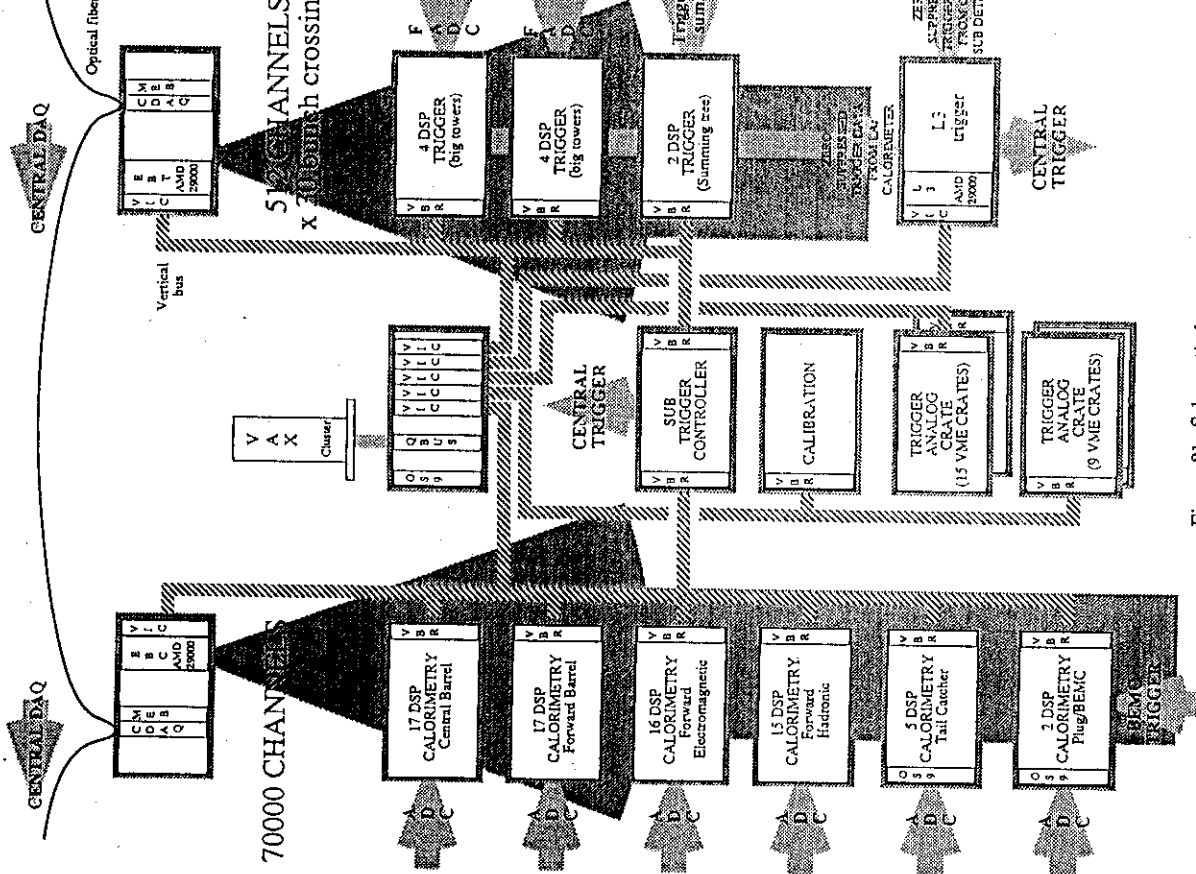


Figure 21: Schematic layout of the data acquisition system

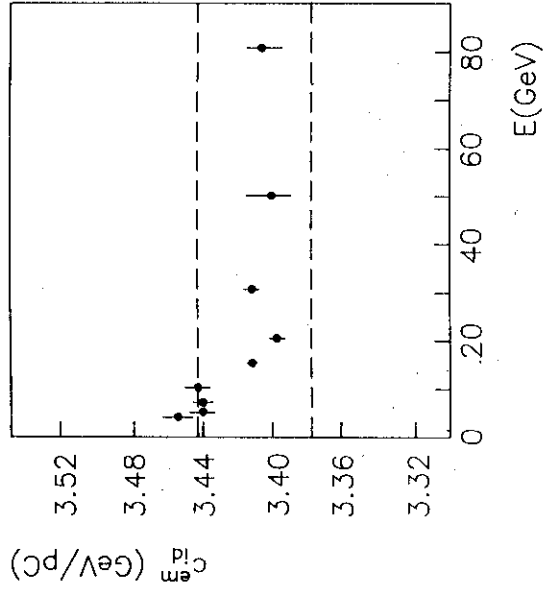


Figure 22: Response as function of energy for electrons.

$$c_{fid}^{HAC} = (c_{fid}^{HAC} / c_{fid}^{EMC}) * c_{fid}^{EMC}$$

The calibration constants for the different wheels vary between 6.7 and 7.6 GeV/pC. The sensitivity of the ratio  $c_{fid}^{HAC} / c_{fid}^{EMC}$  to cut-off parameters is a further error source. The estimate of the systematic error is  $\sim 4\%$ . The direct measurement of the response of hadronic calorimeter to electrons will reduce the contribution of this error source to  $\sim 2\%$ .

## 8.2 Results from the CERN calibration runs

We reported on several tests of H1 prototype calorimeter in refs. [41]-[45]. Meanwhile general H1 stacks were calibrated in eight characteristic configurations representing a full coverage  $\theta$  and all important crack configurations. In the following we summarize some typical results. They are compared to a detailed Monte Carlo simulation of the CERN testbeam set-up with all details of the construction elements have been included. For further results on the calibration by testbeam results and simulation see refs. [11, 35]

Figure 22 shows the linearity of the response of the FB calorimeter module w.r.t. the electron energy for the data. The  $\pm 1\%$  region is shown as well. In order to extract the calibration constant, all corrections due to e.g. noise cuts, inactive material in front of the calorimeter module, restriction to a specific fiducial volume have been taken into account [37]-[40].

Figure 23 shows the energy resolution  $\sigma/E$  for electrons in the energy range 3.7 - 80 GeV data and Monte Carlo events. A fit (solid line) using  $\sigma/E = \sqrt{A^2/E + B^2/E^2 + C^2}$  with  $A = (11.16 \pm 0.05) \cdot 10^{-2} \sqrt{\text{GeV}}$ ,  $B = (152 \pm 4) \text{ MeV}$  and  $C = (0.64 \pm 0.07) \cdot 10^{-2}$ . The result of a corresponding fit to the Monte Carlo data (dashed line) is within the errors computed.

- The nominal capacity to calibrate the electronic chain is 47 pF, in reality small deviations up to 0.6 % are observed. Each channel is individually corrected.

• Due to the pollution of the liquid argon and the finite electric field corresponding to the voltage of 2.5 kV applied to the liquid argon gaps, only a fraction of the deposited charge contributes to the signal. The relation used between the detected charge  $Q_d$ , the maximum available charge  $Q_0$ , the gap thickness  $d$  and the mean free path length  $\lambda$  for absorption of electrons by impurities is given by [36]

$$Q = 2 * Q_0 * (\lambda/d) * (1 - (\lambda/d)) * (1 - e^{-(d/\lambda)})$$

Expressing the losses in oxygen equivalent terms, one can use the relation

$$\lambda = \alpha * E / p$$

$$\alpha = (0.15 \pm 0.03) \text{ [(ppm * cm) / (kV / cm)]}$$

to correct for these losses. Depending on the experimental conditions 5 - 10% of the signal are lost due to electron capture. The time dependence of the pollution was carefully monitored and the corresponding correction applied.

- A Monte Carlo simulation of the detector setup at the CERN beam includes effects due to dead material in front, detector imperfections and noise cuts. It was used to determine the energy  $E_{det}$  deposited in the calorimeter. The careful comparison of the observed and simulated energy deposition in different parts of the detector allows to cross-check the reliability of the Monte Carlo simulation. It has been proven that the calibration constant  $c_{fid}$  depends neither on the cut-off energies used in the Monte Carlo simulation nor on the applied noise cuts.

• The Monte Carlo simulation was also used to correct the detected charge for deviations of the gap thickness from its nominal value. These deviations influence the observed signal due to the change of the effective electric field and the charge produced. These effects compensate partially. The correction which amounts to  $\sim 1\%$  was determined by considering the shower shape as given by the Monte Carlo simulation.

- The deviation of the lead thickness from the nominal value results in a correction of  $\sim 0.2\%$ .

The overall calibration constants  $c_{fid}^{EMC}$  for the different wheels of the electromagnetic calorimeter were measured at different energies. They range from 3.41 to 3.62 GeV/pC [37]-[40]. The differences are a measure of the presently existing systematic uncertainties which are of the order of  $\sim 3\%$ . Further studies of the calorimeter performance are under way in order to identify the source of the observed discrepancies.

**Electromagnetic scale for hadronic calorimeters** For the hadronic stacks no calibration data with electrons are presently available, they will be determined in the near future. Presently we take the computed ratio of the response to electrons of the hadronic and the electromagnetic stacks to determine the ideal electromagnetic scale of the hadronic stacks  $c_{fid}^{HAC}$ . The response is determined by detailed Monte Carlo simulations where the influence of geometry, cut-offs, granularity and the version of the simulation program (EGS4, GEANT) has been carefully studied:

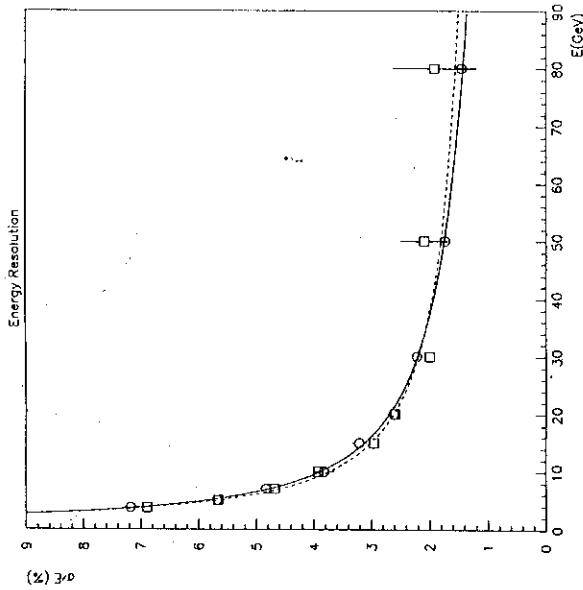


Figure 23: Energy resolution  $\sigma/E$  for electrons as function of energy from the test beam (open circles) and from Monte Carlo simulations (squares).

with the data.

For pions, a novel  $\pi^0$ -weighting technique has been developed ([46]-[48]). A non-linear energy-to-charge relation for the electromagnetic and hadronic calorimeter has been used:

$$E(Q)/Q = [A_1 \cdot e^{-A_2(Q/V)} + A_3]_{EMC} + [B_1 \cdot e^{-B_2(Q/V)} + B_3]_{HAD}$$

Six parameters had to be defined. The energy dependence of these constants has been fully parameterized. The resulting deviation from linearity is shown in Figure 24 for  $\pi^0$ 's of the test beam in the FB/OF stacks. On average, the deviation is within  $\pm 1\%$ , except for energies  $E \leq 20$  GeV where  $\pm 2\%$  is obtained. Figure 25 shows the energy resolution  $\sigma/E$  for pions in the energy range 3.7 - 170 GeV. A fit (dashed line) using  $\sigma/E = \sqrt{A^2/E + B^2/E^3 + C^2}$  yields  $A = (46.1 \pm 0.7) \cdot 10^{-2} \sqrt{\text{GeV}}$ ,  $B = (730 \pm 30)$  MeV and  $C = (2.6 \pm 0.2) \cdot 10^{-2}$ .

These calibration results show that the H1 calorimeter will achieve the performance requirements given in Sect. 2.

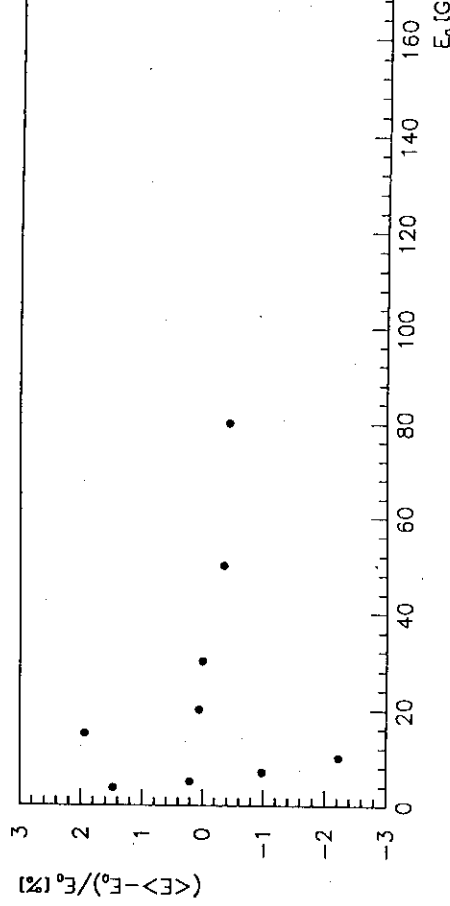


Figure 24: Response as function of energy for  $\pi^0$ 's of the test beam.

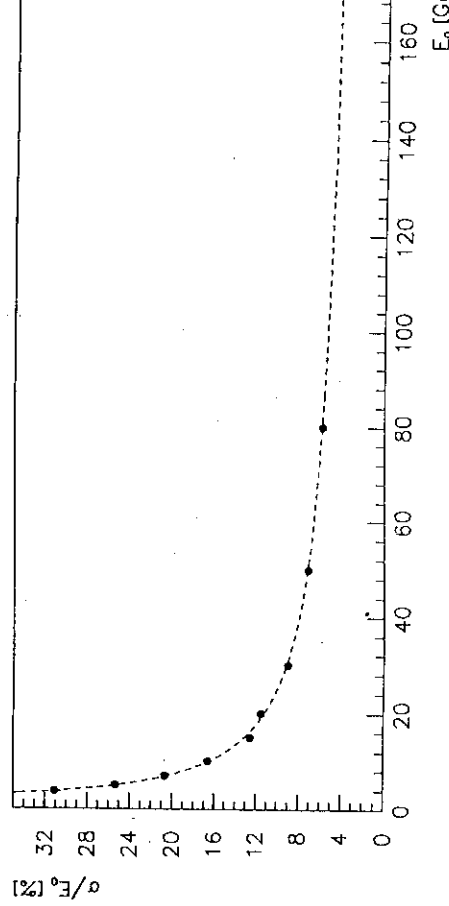


Figure 25: Energy resolution as function of energy for  $\pi^0$ 's of the test beam.

Calorimeter	CB	IF
Electromagnetic	34 MeV / 0.33 Mip's	10 MeV / 0.10 Mip's
Hadronic	28 MeV / 0.15 Mip's	18 MeV / 0.11 Mip's

Table 9: Electronic noise ( $1\sigma$ ) in the electromagnetic and hadronic sections of the central barrel and inner forward modules in units of deposited energy and of minimum ionizing particles.

### 8.3 Results from cosmic ray runs and charge collection efficiency

Cosmic data have been taken with the H1 detector at DESY during a one year period in 1991/92. Several million cosmic triggers have been recorded. Triggers relevant for the analysis of cosmic tracks in the liquid argon calorimeters were

- a track crossing a 16 cm diameter proportional chamber in the central tracking detector
- a track passing through the forward part of the instrumented iron yoke and through the above mentioned proportional chamber

The first trigger provides good coverage of the top and bottom modules of the CB wheels, while the second one provides tracks in the forward modules with vertical plate orientation (FB, IF/OF wheels).

The analysis is based on pattern recognition in the liquid argon calorimeter itself where a cluster method has been used. Muon track candidates were required to deposit a signal above noise threshold in four layers, at least one in the electromagnetic and two in the hadronic section. The noise threshold was symmetric around  $\pm 1.5\sigma$ , i.e. signals above  $1.5\sigma$  and below  $-1.5\sigma$  were kept in an area of 3 by 3 cells around the crossing point of cluster axis and read-out layer. The negative noise provides an automatic compensation of the positive noise contribution to the layer signal. In Tab. 9 the noise level is given for two typical parts of the H1 calorimeter, a low capacity part (IF) and a high capacity one (CB) in terms of deposited energy (see also Sect. 5). It is also compared to the energy deposition of a minimum ionizing particle. Figure 26 shows the charge response in a hadronic layer of a central barrel module of the liquid argon calorimeter [49].

Data taken at different high voltage settings allow to measure the charge collection efficiency as function of the high voltage applied to the gaps. Figure 27 shows high voltage curves in the central barrel hadronic modules. A Monte Carlo correction for the shift of the mean response due to pattern recognition in the presence of noise has been applied. This correction depends on the signal/noise ratio and amounts up to -35% at the lowest high voltage setting (150 V). A fit to the parametrization [36] yields a contamination of  $P = (0.55 \pm 0.14)$  ppm oxygen equivalent corresponding to a charge collection efficiency at 1500 V of  $Q(1.5\text{ kV}/Q_\infty = 0.944 \pm 0.014$ . The errors are estimated from the dispersion of the fit results for the different wheels.

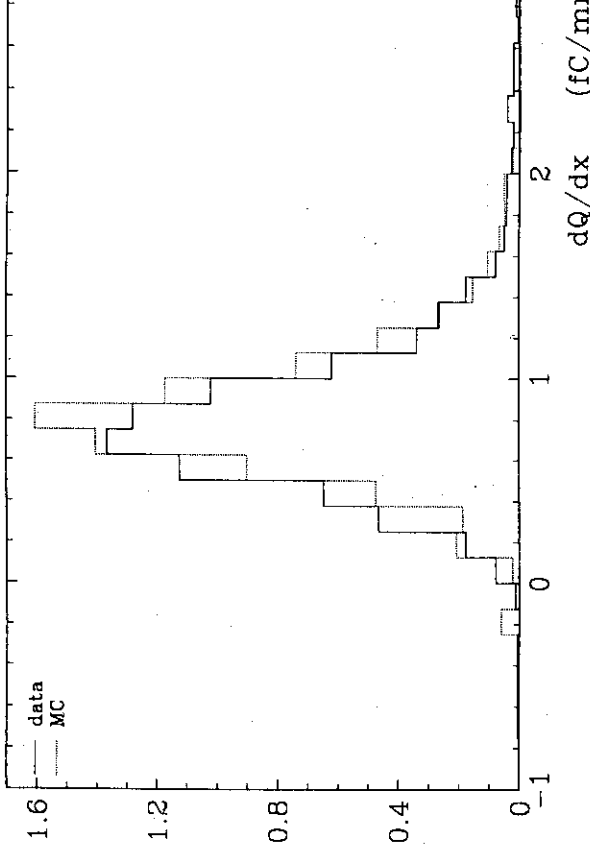


Figure 26: Charge response in a hadronic layer of a central barrel module. The full (dot) histogram shows data (Monte Carlo). In the Monte Carlo simulation noise has been added using random trigger events.

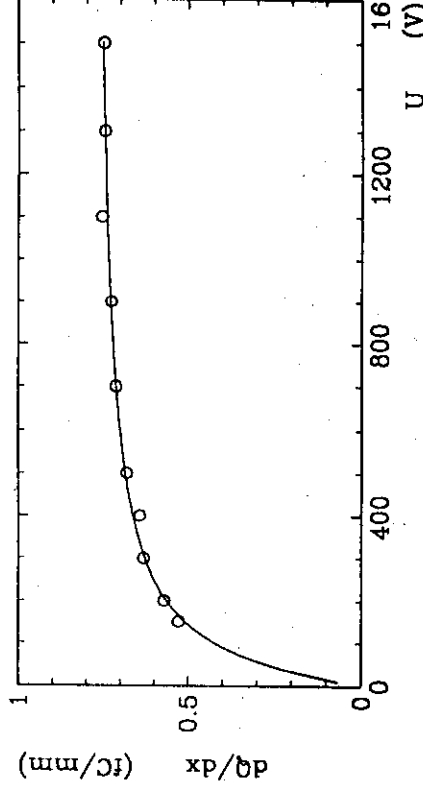


Figure 27: The average charge response in the hadronic layers of the hadronic central barrel wheel 3 as function of high voltage. Superimposed is a fit using the parametrization discussed in the text.

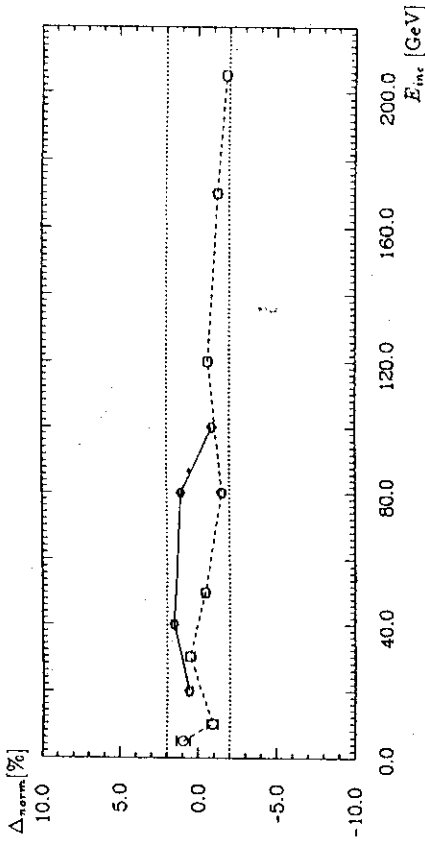


Figure 28: Linearity for simulated charged  $\pi$ 's (circles) and u-quark jets (diamonds).

#### 8.4 Expected performance

The expected performance of the calorimeter has been studied with a full simulation of the liquid argon calorimeter including noise as measured with the full detector at the HERA storage ring. As previously shown, the Monte Carlo simulation agrees with both the calibration data from CERN and with the cosmic data. This gives us confidence to use it for predictions of the expected performance at HERA. We conclude that the calorimeter fulfills the requirements in particular for the constant terms in the energy resolution and homogeneity of the response. The energies of both u-quark jets and single  $\pi$ -mesons which hit the calorimeter in the region of full acceptance are reconstructed with a precision of better than 2% (Fig. 28). If no weighting is applied the reconstructed energy deviates up to 50% from the generated energy. The resolution achieved is shown in Fig. 29. The ability to correct for losses in the cracks of the calorimeter is demonstrated in Fig. 30 for charged  $\pi$ 's which hit the calorimeter at different polar and azimuthal angles. The azimuthal angular interval shown corresponds to 2 half stacks. The required precision of  $\pm 2\%$  is achieved in nearly the full angular range. The losses in the crack are fully corrected, while small deviations from the nominal value are still observed at a polar angle around  $85^\circ$ . The data collected at the HERA storage ring will help to check this result of a detailed detector simulation.

Summarizing the results one concludes that the original design goal of a homogeneous calorimeter has in principle been achieved. Full verification of the calibration by HERA data is in progress.

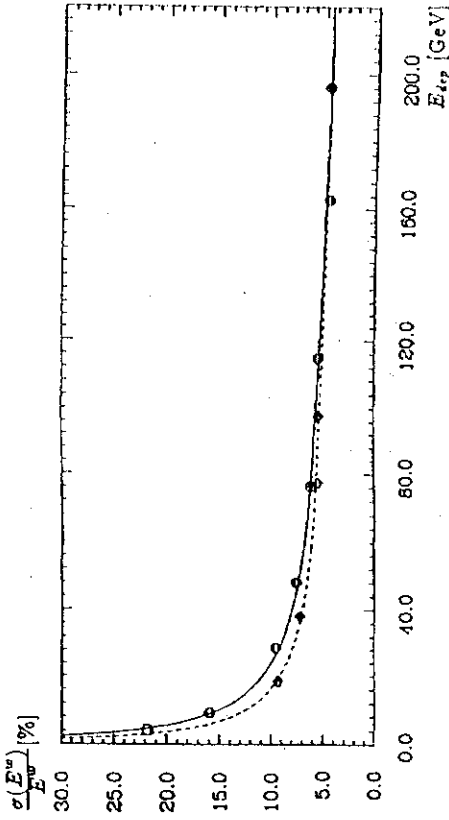


Figure 29: Energy resolution for simulated charged  $\pi$ 's (circles) and u-quark jets (diamonds).

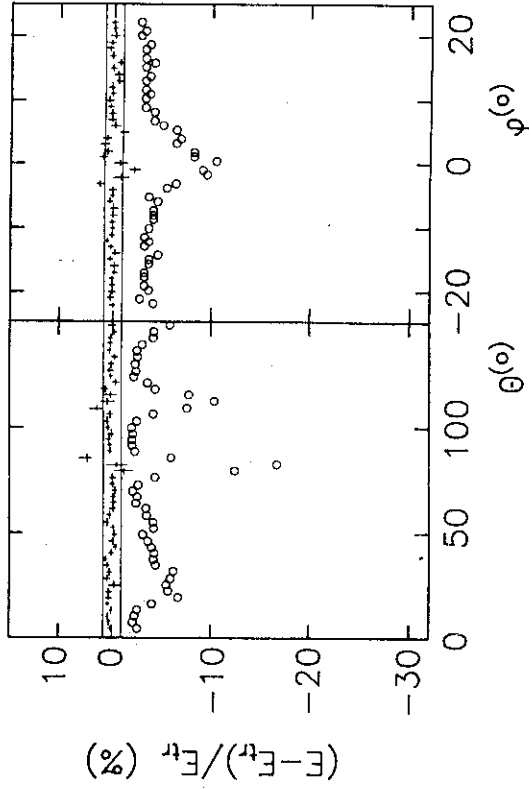


Figure 30: Response of the calorimeter to 20 GeV  $\pi$ 's before (circles) and after (bars) applying crack corrections as a function of the polar ( $\theta$ ) and of the azimuthal ( $\varphi$ ) angle.

## 9 Conclusion

The construction of the H1 liquid argon calorimeter has been finished in December 1990. It was immediately cooled down. In the meantime three cosmic ray runs allowed to establish the proper operation of the detector, the electronics, the trigger and the data acquisition system. In the first physics run which started in June 1992 reliable data were taken. A deep inelastic neutral current event recorded during this data taking period is shown in Fig. 31. The performance of the liquid argon calorimeter has reached its design specifications and leads to physics results in a space-time regime which was not accessible to experiments up to now.

## 10 Acknowledgement

We appreciate the immense effort of the technical staff of the participating laboratories who designed, constructed and maintained the detector. We thank the funding agencies for financial support of this experiment. The non-DESY members of the collaboration also want to thank the DESY directorate for the hospitality extended to them. We acknowledge the help of CERN in providing beam time for the calibration runs. The help of the computing centres at DESY and at CERN is appreciated.

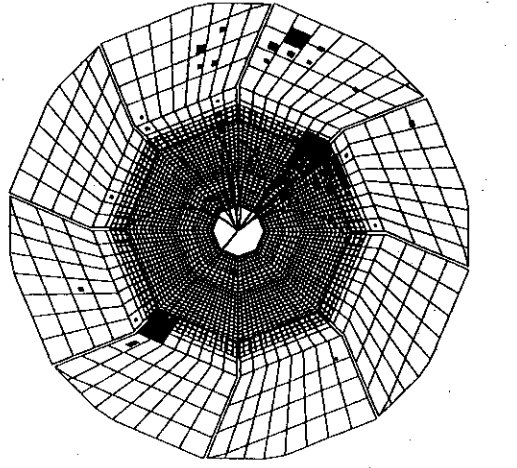
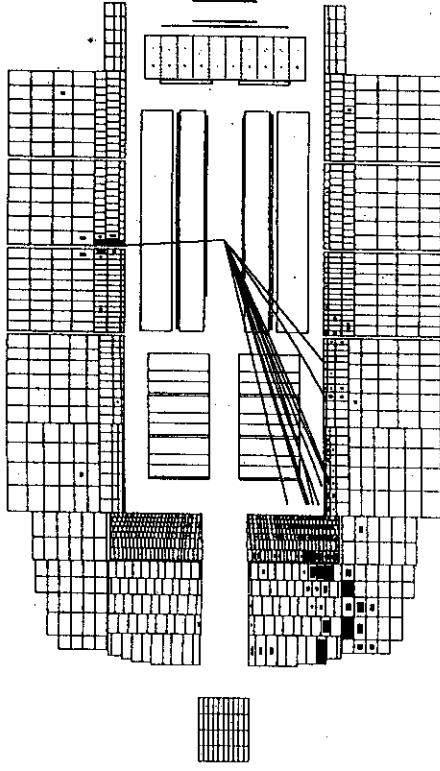


Figure 31: One of the first deeply inelastic neutral current events recorded with the H1 calorimeter ( $Q^2 = 2600 \text{ GeV}^2$ ).

## References

- [1] H1 Collaboration, Technical proposal for the H1 Detector. DESY (1986)
- [2] H1 Collaboration, Technical progress report 1987. DESY (1987)
- [3] H1 Collaboration, Technical progress report 1988. DESY (1988)
- [4] H1 Collaboration, Technical progress report 1989. DESY (1989)
- [5] H1 Collaboration, Technical progress report 1990. DESY (1990)
- [6] Proceedings of the HERA Workshop 1987, editor R.D. Pececi. DESY (1987)
- [7] Physics at HERA, Proceedings of the HERA Workshop 1991, editors W. Buchmüller and G. Ingelman. DESY (1991)
- [8] 'Graphe de Commande Etape Transition', Function diagram defined by French Norm: NF C03-190 (1982)
- [9] V. Radeka and S. Rescia, Speed and noise limits in ionization chamber calorimeters. Nucl.Instr.&Meth. **A265** (1988), 228
- [10] J. Thomas and D.A. Imel, Recombination of electron-ion pairs in liquid argon and liquid xenon. Phys.Rev. A **36** (1987), 614
- [11] H1 Calorimeter Group, Test beam results and calibration of the H1 liquid argon calorimeter for electrons. (In preparation) (1993)
- [12] V. Brisson, Tower and pad segmentation of the H1 liquid argon calorimeter. H1 Internal Report H1-TR-114 (1987)
- [13] J. Antos et al., Manufacture of read-out boards for the H1 liquid argon calorimeter. Nucl.Instr.&Meth. **A302** (1991), 277
- [14] H. Brettel et al., The electronic system for the H1 liquid argon calorimeters. Progress Report. H1 Internal Report H1-TR-115 (1987)
- [15] H. Oberlack and P. Ribarics, Minimal and maximal signals in the H1 liquid argon calorimeter. H1 Internal Report H1-03/89-106
- [16] V. Brisson and A. Reboux, From the physical tower segments to the electronic channels, H1 Internal Report H1-05/89-110
- [17] V. Brisson, H. Oberlack and P. Ribarics, Mapping and adjustment of the calorimeter electronic channels up to ADC's. H1 Internal Report H1-02/89-104
- [18] W.J. Willis and V. Radeka, Liquid argon ionization chambers as total-absorption detectors. Nucl.Instr.&Meth. **120** (1974), 221
- [19] H.J. Behrend et al., CELLO - A new detector at PETRA. Phys. Scripta **23**, 610 (1981)
- [20] W. Pimpl and P. Weiffbach, Preamplifier am H1 Kalorimeter. MPI Internal Report, H1-MPI-057 (1987)
- [21] H. Brettel, W. Pimpl and P. Weiffbach, Shaper for the H1 Calorimeter. MPI Internal Report, H1-MPI-058 (1987)
- [22] R. Bernier et al., H1 calorimeter electronics. H1 Internal Report H1-07/92-237
- [23] R. Bernier et al., Pedestal drift and cable pickup problems in multiplexed analog signal transmission. NS Symposium 34, San Francisco. IEEE Transactions on Nuclear Science, Vol.35, page 131 (1988)
- [24] DSP8150 by CES, Geneva, following a DAPNIA design.
- [25] D. Breton et al., H1 calorimeter calibration electronics. H1 Internal Report H1-04/92-222
- [26] C. Arnault et al., Correction for missing cold calibration generators in the H1 liquid argon calorimeter. H1 Internal Report H1-12/91-203
- [27] A. Jacholkowska et al., Electronic calibration result from October - November cosmic test. H1 Internal Report H1-02/92-209
- [28] C. Pascaud et al., Adjustment of the calibration timing parameter in liquid argon calorimeter to cosmic runs data. H1 Internal Report H1-04/92-222
- [29] A. Jacholkowska et al., Timing in the liquid argon calorimeter acquisition branch. H1 Internal Report H1-06/92-229
- [30] G. Grindhammer et al., The first level liquid argon calorimeter trigger - Physics requirements. H1 Internal Report H1-TR-300 (1987)
- [31] H. Brettel et al., The first level liquid argon calorimeter trigger - Technical realisation. H1 Internal Report H1-TR-301 (1987)
- [32] AM29000 32-bit Streamlined Instruction Processor, Advanced Micro devices.
- [33] VRTX32/29000 Real-time Executive for AM29000, Ready system.
- [34] F. Descamps and C. Vallée, Acquisition for the calorimeters of H1. Proceedings of the Int. Conf. on Calorimetry in High Energy Physics, Corpus Christi (1992)
- [35] H1 Calorimeter Group, Results from pion calibration runs for the H1 liquid argon calorimeter and comparisons with simulations. DESY 93-047 (1993) and submitted to Nucl.Instr.&Meth.
- [36] W. Hofmann et al., Production and transport of conduction electrons in a liquid argon ionization chamber. Nucl.Instr.&Meth. **135** (1976), 151
- [37] J. Gayler, H. Küster and P. Loch, Determination of the electromagnetic scale for the calorimeter. H1 Internal Report H1-04/91-171
- [38] J.-F. Laporte, Diffusion profondément inélastique à HERA et calibration absolue de mesure en énergie d'un électron dans le calorimètre à argon liquide de l'expérience E1. Thèse de Doctorat de l'Université de Paris-Sud (1991)
- [39] K. Borras, Aufbau und Kalibration eines Flüssig - Argon - Kalorimeters im H1 Detektor. Doktorarbeit Universität Dortmund (1992)

- [40] P. Hartz, Kalibration eines Blei - Flüssig - Argon - Kalorimeters mit Elektronen für das H1 Experiment. Doktorarbeit Universität Dortmund (1993)
- [41] W. Braunschweig et al., Results from a test of a Pb-Cu liquid argon calorimeter. Nucl.Instr.&Meth. **A265** (1988), 419
- [42] W. Braunschweig et al., Results from a test of an iron streamer tube calorimeter. Nucl.Instr.&Meth. **A270** (1988), 334
- [43] W. Braunschweig et al., Performance of a Pb-Cu liquid argon calorimeter with an iron streamer tube tail catcher. Nucl.Instr.&Meth. **A275** (1989), 246
- [44] W. Braunschweig et al., Results from a test of a Pb-Fe liquid argon calorimeter. DESY 89-022 (1989)
- [45] J. Marks, Eigenschaften eines Kalorimeters aus Blei und Kupfer in flüssigem Argon zur Messung hochenergetischer Jets unter besonderer Berücksichtigung einer Reduktion der Schauerfluktuationen. DESY F21-90-01, Thesis, University of Hamburg, 1989. Doktorarbeit Universität Hamburg (1989)
- [46] H. Greif, Untersuchung zur kalorimetrischen Messung von Jeteigenschaften in hochenergetischen Elektron - Proton Speicherring - Experimenten. Doktorarbeit Technische Universität München (1990)
- [47] P. Loch, Kalibration des H1 Flüssig - Argon - Kalorimeters unter Berücksichtigung der Gewichtungsmethode für Teilchen-Jets. Doktorarbeit Universität Hamburg (1992)
- [48] H1 Calorimeter Group, Study of Software Compensation for Single Particles and Jets in the H1 Calorimeter. Contributed paper to the XXV International Conference on High Energy Physics, Singapore (1990)
- [49] J. Stier, Kalibration des H1 Flüssig - Argon - Kalorimeters mit kosmischen Myonen. Diplomarbeit Universität Hamburg (1992)